



저작자표시 2.0 대한민국

이용자는 아래의 조건을 따르는 경우에 한하여 자유롭게

- 이 저작물을 복제, 배포, 전송, 전시, 공연 및 방송할 수 있습니다.
- 이차적 저작물을 작성할 수 있습니다.
- 이 저작물을 영리 목적으로 이용할 수 있습니다.

다음과 같은 조건을 따라야 합니다:



저작자표시. 귀하는 원저작자를 표시하여야 합니다.

- 귀하는, 이 저작물의 재이용이나 배포의 경우, 이 저작물에 적용된 이용허락조건을 명확하게 나타내어야 합니다.
- 저작권자로부터 별도의 허가를 받으면 이러한 조건들은 적용되지 않습니다.

저작권법에 따른 이용자의 권리는 위의 내용에 의하여 영향을 받지 않습니다.

이것은 [이용허락규약\(Legal Code\)](#)을 이해하기 쉽게 요약한 것입니다.

[Disclaimer](#) 

**ACCURATE MEASUREMENT OF
NANOMECHANICAL PROPERTIES USING AFM
FORCE-INDENTATION CURVES: APPLICATION
TO SOFT AND BIOLOGICAL MATERIALS**

Quang Dang Nguyen

School of Mechanical Engineering

University of Ulsan, Korea

**ACCURATE MEASUREMENT OF
NANOMECHANICAL PROPERTIES USING AFM
FORCE-INDENTATION CURVES: APPLICATION
TO SOFT AND BIOLOGICAL MATERIALS**

Supervisor: Prof. Koo-Hyun Chung

A Dissertation

Submitted to

the Graduate School of the University of Ulsan

In partial Fulfillment of the Requirements

for the Degree of

Doctor of Philosophy

by

Quang Dang Nguyen

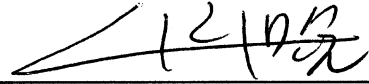
School of Mechanical Engineering

University of Ulsan, Korea

November 2019

**Accurate Measurement of Nanomechanical Properties
Using AFM Force-indentation Curves: Application to
Soft and Biological Materials**

This certifies that the dissertation
of Quang Dang Nguyen is approved.


Committee Chairman: Prof. Doo-Man Chun


Committee Member: Prof. Koo-Hyun Chung


Committee Member: Prof. Sung-Tae Hong


Committee Member: Prof. Dong-Kyu Kim


Committee Member: Prof. Hae-Jin Kim

School of Mechanical Engineering

University of Ulsan, Korea

November 2019

TABLES OF CONTENTS

TABLES OF CONTENTS	i
LISTS OF TABLES.....	iv
LISTS OF FIGURES.....	v
ABSTRACT.....	ix
Chapter 1 Introduction.....	1
1.1 Background and motivation	1
1.2 Objectives of the research	2
1.3 Organization of the research	3
Chapter 2 Literature review	5
2.1 AFM force-indentation curves	5
2.2 Nanomechanical properties measurements using AFM force-indentation curves and related issues.....	6
Chapter 3 Effects of tip shape and friction on nanomechanical properties measurements.....	9
3.1 Experimental details.....	9
3.1.1 Materials	9
3.1.2 Methods	11
3.2 Probe with spherical tip.....	16
3.3 Probe with flat ended tip	19
3.4 Probe with conical tips with rounded apexes	21

3.5 Comparison of measurement results	26
3.6 Summary	32
Chapter 4 Nanomechanical properties measurements of polymer binders for lithium-ion batteries.....	34
4.1 Introduction and objectives	34
4.2 Experimental details	37
4.2.1 Materials	37
4.2.2 Methods	38
4.3 Surface structures	42
4.4 Nanomechanical and adhesion properties	44
4.4.1 Measurement results in air.....	44
4.4.2 Measurement results in electrolyte	47
4.4.3 Effect of electrolyte	49
4.5 Summary	56
Chapter 5 Nanomechanical properties measurements of individual collagen fibrils and collagen matrices	58
5.1 Introduction and objectives	58
5.2 Experimental details.....	60
5.2.1 Preparation of collagen specimens	60
5.2.2 AFM topographical imaging	61
5.2.3 AFM force-indentation curve measurements	62

5.3 Surface structures	63
5.4 Nanomechanical properties	67
5.4.1 Elastic modulus of individual collagen fibrils.....	67
5.4.2 Elastic modulus of collagen matrices	69
5.4.3 Effects of structural modification	71
5.5 Discussion and summary.....	73
Chapter 6 Conclusions and recommendations.....	76
6.1 Conclusions of the research.....	76
6.2 Recommendations for future work.....	78
REFERENCES.....	79

LISTS OF TABLES

Table 3.1 Summary of the elastic moduli determined for the PAA, PVDF, and SBR specimens.....	27
Table 4.1 Summary of the reduced elastic moduli determined for the PAA, PAN, PVA, CMC, and PVDF specimens.....	51
Table 5.1 Summary of the reduced elastic moduli determined for the individual collagen fibrils and collagen matrices with 0%, 20%, and 50% N-solution.....	72

LISTS OF FIGURES

Fig. 1.1. Objective and scope of this research.	3
Fig. 2.1. An example of photo-detector output and force with respect to displacement obtained using AFM. Force is calculated from photo-detector output using deflection sensitivity and spring constant of the cantilever.	6
Fig. 3.1. AFM topography images of the (a) PAA, (b) PVDF, and (c) SBR specimens. ...	11
Fig. 3.2. Photo-detector output with respect to (a) displacement and (b) indentation obtained using probes A, B, C, and D against a bare Si substrate. In (b), cantilever deflection was determined using the photo-detector output and mean of deflection sensitivities from extension and retraction curves ($S_{d,ext}$ and $S_{d,ret}$, respectively), and indentation was obtained by subtracting the cantilever deflection from piezo displacement.	13
Fig. 3.3. Force-indentation curves of the (a) PAA, (b) PVDF, and (c) SBR specimens obtained at speeds ranging from 50 nm/s to 500 nm/s using probe D.	14
Fig. 3.4. AFM images of the PAA, PVDF, and SBR specimens before and after force-indentation curve measurements using probes (a) C and (b) D. AFM images after the measurements subtracted from those obtained before the measurements were included for comparison.	15
Fig. 3.5. (a) SEM images of probe A, and (b) force-indentation curves, and (c) histograms of mean elastic modulus of the PAA, PVDF, and SBR specimens obtained using probe A.	18
Fig. 3.6. (a) SEM images of probe B, and (b) force-indentation curves of the PAA, PVDF, and SBR specimens obtained using probe B.	19

Fig. 3.7. (a) SEM images of probe C, and (b) force-indentation curves, and (c) histograms of mean elastic modulus of the PAA, PVDF, and SBR specimens obtained using probe C.22

Fig. 3.8. (a) SEM images of probe D and (b) upper and (c) lower bounds of tip radius and half apex angle of probe D determined from the SEM image considering the blurring boundary.23

Fig. 3.9. (a) Force-indentation curves and (b) histograms of mean elastic modulus of the PAA, PVDF, and SBR specimens obtained using probe D.24

Fig. 3.10. Examples of abnormal force-indentation curves obtained from the (a) PAA, (b) PVDF, and (c) SBR specimens using probe D.25

Fig. 3.11. Force-indentation curves of the PAA, PVDF, and SBR specimens obtained from instrumented indentation.28

Fig. 3.12. Residuals between indentation data and model fits normalized by the indentation depth for probes (a) A, (b) C, and (c) D.29

Fig. 3.13. Ratio of elastic moduli of the specimens determined from the extension and retraction curves, $E_{s,ret}/E_{s,ext}$, as a function of the ratio of contact stiffness to flexural stiffness of probes, k_{con}/k_N30

Fig. 3.14. Examples of friction loops of the PAA, PVDF, and SBR specimens slid against a Si probe under a 10 nN normal force.31

Fig. 4.1. AFM images of the PAA, PAN, PVA, CMC, and PVDF specimens obtained in (a) air and (b) electrolyte, and (c) RMS surface roughnesses of the specimens in air and electrolyte.42

Fig. 4.2. (a) Force-indentation curves and (b) histograms of the means of reduced elastic moduli determined from extension and retraction curves for the PAA, PAN, PVA, CMC, and PVDF specimens in air.45

Fig. 4.3. Works of adhesion of the PAA, PAN, PVA, CMC, and PVDF specimens determined from extension and retraction curve fits (E_s^* and γ are unknown parameters for curve fitting) and from the pull-off forces (Eq. (3.4)) based on the JKR model.47

Fig. 4.4. (a) Force-indentation curves and (b) histograms of the means of reduced elastic moduli determined from extension and retraction curves for the PAA, PAN, PVA, CMC, and PVDF specimens in electrolyte.48

Fig. 4.5. Friction loops of the (a) PAA, (b) PAN, (c) PVA, (d) CMC, and (e) PVDF specimens, and (f) summary of the friction force of the specimen obtained under a 10 nN normal force in air and electrolyte.52

Fig. 4.6. Examples of force-indentation curves of the PAA, PAN, PVA, CMC, and PVDF specimens obtained using instrumented indentation.53

Fig. 4.7. The capacity retention of Si anodes containing PAA, PAN, PVA, CMC, and PVDF binders after 50 charge/discharge cycles along with the reduced elastic moduli of the specimens in electrolyte. The capacity retention is defined as percentage ratio of the capacity after 50 charge/discharge cycles to the initial capacity.54

Fig. 5.1. (a) AFM height images, (b) AFM amplitude images, and (c) D-bandings of the collagen fibrils with 0%, 20%, and 50% N-solution.64

Fig. 5.2. (a) AFM height images, (b) fibril widths, and (c) material ratio curves of the collagen matrices with 0%, 20%, and 50% N-solution. The material curve represents the percentage of material traversed in relation to the area covered.66

Fig. 5.3. (a) Force-indentation curves and (b) mean elastic modulus of the collagen fibrils with 0%, 20%, and 50% N-solution.67

Fig. 5.4. AFM amplitude images of the collagen fibrils with 0%, 20%, and 50% N-solution (a) before and (b) after force-indentation curve measurements.68

Fig. 5.5. (a) Force-indentation curves, (b) mean elastic modulus, and (c) works of adhesion of the collagen matrices with 0%, 20%, and 50% N-solution. In (a), the black arrows indicate that the number of adhesion events is higher for matrices with 20% and 50% N-solution than that of 0% N-solution.69

Fig. 5.6. Examples of force-indentation curves measured continuously at same locations on the collagen matrices with (a) 0%, (b) 20%, and (c) 50% N-solution. 70

ABSTRACT

Atomic force microscopy (AFM) has widely been used for understanding of mechanical properties in conjunction with surface structure and topography at the nano-scale. To probe the mechanical properties using an AFM, a force-indentation curve that represents relationship between applied force by an AFM probe and deformation of a target specimens has generally been obtained. Then, force-indentation data can be interpreted based on a contact model to determine the mechanical properties of target specimen. However, measurements of the mechanical properties from a force-indentation curve is not always straightforward. To improve the accuracy of mechanical properties measurements using AFM force-indentation curves, systematic approach based on understanding of the interaction between AFM probe and specimen is considerably needed.

In this research, effect of tip shapes on nanomechanical properties measurement using AFM was systematically investigated. The force-indentation curves were obtained using different AFM probes with spherical and flat-ended tips, and conical tips with rounded apices with an aim to provide useful information for selection of the probe and for better interpretation of force-indentation data. These probes were modeled as a sphere, flat punch, and hyperboloid, respectively, after careful characterization to determine the elastic modulus based on contact models. The effect of friction-induced hysteresis in the force-indentation curve was also experimentally observed and discussed. It was found that the flat ended tip was prone to misalignment between the tip flat end and specimen surface. The imperfect contact in turn caused difficulty in interpretation of force-indentation data based on the contact model. In addition, a hysteresis was consistently observed in force-indentation data obtained using the spherical tip and the conical tips with rounded apices, feasibly due to effect of friction between the tip and specimen. As a result, a significant

different (up to 100%) between elastic moduli determined from extension and retraction curves were observed when the force-indentation data was interpreted using the contact model. Considering that uncertainties associated with tip shape, friction, and force and indentation measurements, the probe with relatively large tip radius (e.g., ~ 30 nm) and minimal spring constant was recommended for mechanical properties measurement of specimen with a few GPa elastic modulus.

Based on the understanding of the effects of tip shape and friction on the force-indentation data, AFM force-indentation curves were used to quantitatively determine the nanomechanical properties of polymer binders for lithium-ion batteries (LIBs). In particular, the effect of electrolyte on the mechanical properties of polymer binders were systematically investigated. The experimental results showed that the mechanical properties of polymer binders in electrolyte were smaller by factors of 3–259 than those in air, likely due to swelling of polymer. It was also found that the effect of electrolyte on the surface roughness may be dependent on the structure of the polymer specimens. In addition, significant hysteresis was observed in the force-indentation curves obtained in air due to effect of friction, however, this effect was negligible for data obtained in electrolyte which may be due to significant decrease in friction characteristics of the specimens. The results suggest that understanding of the friction characteristics of the system may be helpful to minimize or avoid the friction-induced hysteresis in force-indentation curves for more accurate measurement of the mechanical properties. The outcomes also provide useful information for development of polymer binders for improved electrochemical stability of electrodes for LIBs based on understanding of the effects of electrolyte on material properties of polymer binders. In addition, the approach of this work can also be used for mechanical properties measurements of soft materials using AFM with improved accuracy.

As a widely used approach to characterize the nanomechanical properties of biological materials, AFM-based indentation technique was also used to understand the mechanical properties of fibrillar materials such as collagen. In particular, the structure of collagen fibrils was controlled into bundles by incorporating the sulfate anion during the polymerization process of collagen. The effects of structural change of collagen fibrils on their mechanical properties were then experimentally investigated using the AFM. Force-indentation curves were obtained on individual collagen fibrils, as well as on matrices of collagen fibrils. The structures of specimens were also carefully observed and characterized, given that structural property is a key factor that may affect the mechanical properties of materials with fibrillar structures. It was shown that the width of collagen bundles increased with increasing concentration of sulfate anion. Also, the mechanical properties of the collagen matrices were found to be more dependent on the structure of matrix network than the mechanical properties of individual collagen fibrils alone. The approach may add in more accurate measurement of mechanical properties of biological materials using AFM. Also, the outcomes provide information to help understand the nanomechanical properties of collagen that can be sensed by cells and influence cell behavior.

Chapter 1 Introduction

1.1 Background and motivation

Quantitative understanding of mechanical properties of materials associated with their structures and surface morphology at nano-scale is of importance across broad spectrums of industrial, biomedical, and energy applications. For example, the cycling performance of lithium-ion batteries (LIBs) is dependent on the mechanical properties of polymer binders [1,2]. Also, the mechanical properties of collagen fibrils can play a critical role in determining cell behaviors [3]. Atomic force microscopy (AFM) has widely been used as a tool to measure the nanomechanical properties as well as to observe the surface topography with high spatial resolution based on the interactions between a sharp tip and a specimen. In addition, high sensitivity to small forces allows the AFM to non-destructive investigate materials with relatively low mechanical properties. Furthermore, the ability to perform experiments in controlled environments (e.g., temperature, humidity, liquid) of AFM is also an advantage for properties measurements of various materials. In this regard, the AFM has been extensively used to study the nanomechanical properties of various materials, especially soft materials such as polymers and biological materials [1-4].

To probe the mechanical properties using an AFM, a force-indentation curve (or force spectroscopy) which represents the deformation of a target specimen with respect to an applied force is generally obtained. Then, mechanical properties such as elastic modulus can be determined from a relationship between applied force and deformation based on contact models [5]. In addition, mechanical properties of the target specimen can be determined from using a reference specimen or a set of reference specimens with accurately known mechanical properties [6,7]. Furthermore, various AFM-based techniques such as contact resonance force microscopy [8,9] and torsional harmonic AFM [10] have been

demonstrated for mapping of the mechanical properties. However, it is not always straightforward to accurately measure the nanomechanical properties using an AFM due to uncertainties that can be associated with tip characterization and data interpretation [4,11-13], and interfacial behaviors between AFM tip and specimen [14-20]. Also, inappropriate force calibration procedures and instrumental uncertainties (e.g., hysteresis or creep of piezo scanner) of AFM can readily affect the measurement accuracy [21,22]. The motivation of this research is to gain better understanding of nanomechanical properties measurements using AFM.

1.2 Objectives of the research

In this research, the objective is to provide useful information for obtaining accurate nanomechanical properties measurements using AFM, based on better understanding of the interaction between AFM probe and specimen. To do so, force-indentation data was obtained using AFM tips with different shapes, with an aim to systematically investigate the effects of tip shape and friction on nanomechanical properties measurements. Based on the useful information attained from this investigation, the force-indentation curve was used to understand the mechanical properties of soft and biological materials. In particular, the nanomechanical properties of polymer binders for LIBs were quantitatively investigated to accumulate information for design of polymer binders for electrodes of LIBs with improved cycling stability. Also, as an application of AFM force-indentation curve measurements to biological materials, especially for materials with fibrillar structures, the nanomechanical properties of collagen matrices with different structures were assessed with an aim to gain better understanding on how cells sense and response to the changes in

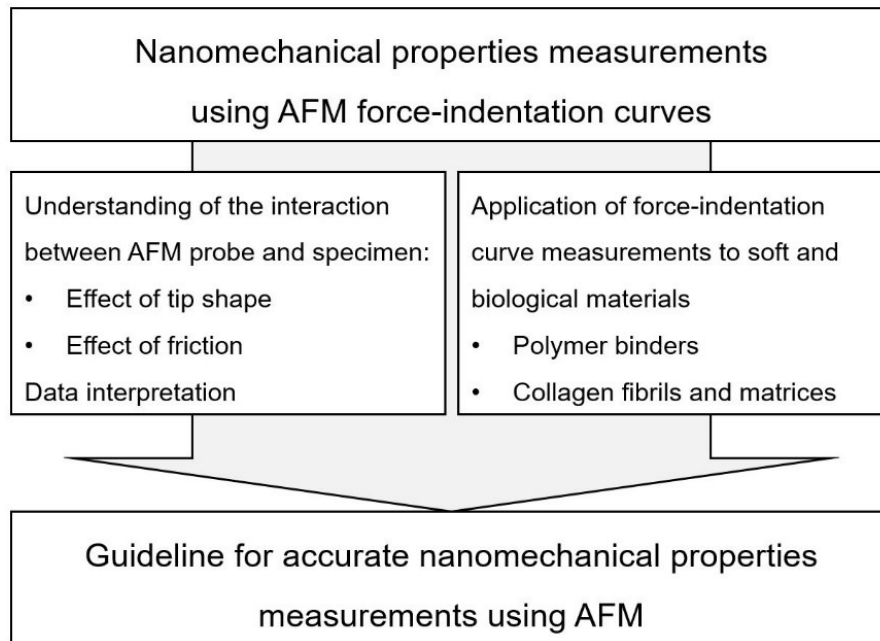


Fig. 1.1. Objective and scope of this research.

structure and mechanical properties of collagen. The objective and scope of this research are summarized in Fig. 1.1.

1.3 Organization of the research

Following the introductory remarks of this chapter, chapter 2 summarizes the literature review about measurements of nanomechanical properties based on AFM force-indentation curves and related issues. Then, in chapter 3, the effects of tip shape and friction on nanomechanical properties measurements will be discussed. The aim is to provide useful information for probe selection and for a better understanding of force-indentation data regarding friction-induced hysteresis, which may be useful for more accurate nanomechanical property measurements using an AFM.

Based on the approach used in chapter 3, in chapter 4, the nanomechanical properties in air and in electrolyte of various polymer binders for LIBs were quantitatively assessed

using the AFM. The effect of friction on force-indentation curve measurements in air and in electrolyte is also discussed in this chapter. Furthermore, works of adhesion of polymer binders were quantitatively measured based on the contact model. In addition, the experimental procedure for force-indentation curve measurements in liquid environment using AFM is also presented. The results can be useful to gain a better understanding of the nanomechanical and adhesion properties of various polymer binders of LIBs and, therefore, provide useful information for selection of polymer binders.

Chapter 5 presents the investigation of the nanomechanical properties of collagen. In particular, the force-indentation curves on individual collagen fibrils and matrices network of collagen fibrils with different structures were obtained and interpreted. Also, the mechanical properties of collagen specimens were correlated with their structures to understand the relationship between structural and mechanical properties. The results can provide further understanding of the effects of changes in collagen structures on cell behaviors.

Chapter 6 presents the major conclusions of this research along with recommendations of future works. The approaches proposed in this work are expected to aid in useful information for accurate measurements of the nanomechanical properties of soft and biological materials. It is suggested that hysteresis due to friction should be avoided or minimized for accurate determination of elastic modulus from a force-distance curve obtained using an AFM. In addition, the discussions for AFM tip characterization and data interpretation, and the experimental procedure for data collection in liquid environment may be helpful to provide information for further studies on nanomechanical properties based on AFM force-indentation curve.

Chapter 2 Literature review

2.1 AFM force-indentation curves

A force-indentation curve is a graph that shows relationship between force experienced by AFM cantilever with respect to the deformation of a target specimen. To obtain the force-indentation curve, initially, the photo-detector output and displacement of piezo actuator should be recorded by approaching the tip and specimen towards each other until contact occur and then separate them. After that, photo-detector output-displacement curve will be converted into force-displacement curve using deflection sensitivity and spring constant of the cantilever. The force-displacement curve is then converted into force-indentation curve by subtracting the cantilever deflection from the displacement.

Figure 2.1 shows an example of AFM photo-detector output-displacement curve. The force calculated using deflection sensitivity and spring constant of the cantilever is also presented in Fig. 2.1. The curve can be separated into two parts based on the movement directions: extension curve in which the tip and specimen approach toward each other, and retraction curve in which the tip and specimen separate from each other. The extension and retraction curves then can be divided into three regions: the zero line, the discontinuities, and the contact regions [4]. As depicted in Fig. 2.1, there is no interaction when the tip is far from surface (region 1), the output signal from the photo-detector is equal to zero. Contact occurs when the gradient of the attractive force exceeds the force constant of the cantilever and causes abruptly snap of the cantilever onto the surface (point 2). In the contact regions (regions 3 and 5), the tip continues to move toward the specimen until a pre-determined output value (point 4). When the target point is reached, the tip starts to retract from the surface until the force constant of cantilever overcomes the pull-off force between the tip and specimen (point 6) and returns to the starting position (region 7).

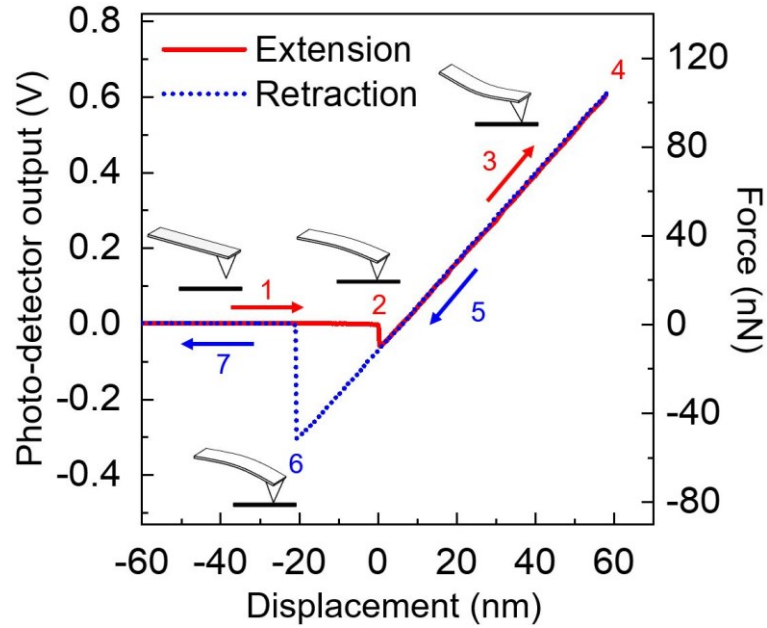


Fig. 2.1. An example of photo-detector output and force with respect to displacement obtained using AFM. Force is calculated from photo-detector output using deflection sensitivity and spring constant of the cantilever.

2.2 Nanomechanical properties measurements using AFM force-indentation curves and related issues

Measurement of mechanical properties using the force-indentation curve often involves a contact model that describes the contact geometry and interaction forces between a tip and a specimen. For example, to describe the contact between a spherical tip and specimen, Hertzian contact model [20] can be applied when the adhesion force is negligible. However, when the adhesion is significant, adhesive contact models should be used. For the case of large adhesion with large tip and compliant specimen, Johnson-Kendall-Roberts (JKR) model [21] can be applied. Also, Derjaguin-Muller-Toporov (DMT) model [22] is more appropriate for small adhesion with small tip and stiff specimen case. In addition, to

understand the contact geometry, the tip should be carefully characterized for appropriate selection of the contact model. Conventional AFM probes have a conical tip with a rounded apex, and the tip has often been modeled as spherical [23,24], parabolic [3,25], hyperbolic [26,27], and conical [28,29] shapes for force-indentation data analysis. In addition, a flat punch model can be used for commercialized AFM probes with flat ended tips or for AFM probes with a tip flattened due to wear [11]. The spherical model is generally employed for colloidal probes where a spherical particle is often attached to the probe to provide a controlled geometry [30,31]. Essentially, the AFM probe should be carefully selected in conjunction with measurement conditions (e.g., applied force and indentation) depending on the expected properties of a target material, so that the contact pressure is large enough for significant indentation within the elastic region to achieve high measurement accuracy and to justify calculation using a contact model [5,13]. The indentation depth should be significantly smaller than the tip radius when using the spherical contact model [32] and, therefore, a probe with a relatively large tip radius (e.g., colloidal probe) is often preferred to obtain a sufficiently large indentation. Also, the tip should be carefully characterized when using the parabolic contact model since an incorrect assumption on tip shape with a paraboloid may cause a relatively large uncertainty in the elastic modulus value when the indentation depth is large [12]. In addition, the indentation should be large enough to minimize the effect of the rounded apex when modeling the conventional AFM probe with a conical tip with a rounded apex as a cone. This suggests that a conical contact model could be more appropriate for soft materials. Furthermore, a flat-ended tip is susceptible to misalignment with respect to the specimen surface, which can cause significant measurement uncertainty due to imperfect contact and, therefore, it may be suitable for extremely flat specimens. In this regard, several studies have been presented to provide guidelines for mechanical property measurement using the force-indentation curve

[4,11,12]. However, it is not always straightforward to select an AFM probe appropriately for force-indentation curve measurements or to determine mechanical properties based on contact models.

Interfacial behavior due to sliding contact between a tip and specimen, such as friction and wear, may significantly affect force-indentation data. For example, the change in tip shape due to wear causes changes in contact geometry between the tip and specimen, which further increases the uncertainty in interpretation using the contact model [14,15]. Considering that the wear rate of the tip increased with a decrease in the tip radius, the tip wear should be more carefully considered at the initial stage of contact, especially for the case of a sharper tip [33,34]. In addition, friction between the tip and specimen in the axial direction causes a torque that opposes the normal bending moment during force-displacement curve measurements and, hence, the signal from the photo-detector can be underestimated and overestimated in extension and retraction curves, respectively [16-20]. Particularly, it was shown that friction coefficient can be determined simultaneously along with force calibration factor [18] or specimen stiffness [20] from the difference in extension and retraction curves. However, the effect of friction on the mechanical property measurements from force-indentation data has not been extensively explored yet.

Chapter 3 Effects of tip shape and friction on nanomechanical properties measurements

3.1 Experimental details

3.1.1 Materials

In this chapter, force-indentation curves were obtained using four different AFM probes with spherical and flat-ended tips, and conical tips with rounded apexes. For the probe with the spherical tip (probe A), an Au spherical particle was attached on a tipless cantilever (TL-NCH, Nanosensors) using a room temperature curable two-components epoxy resin. To do this, the cantilever was first mounted onto the probe holder of the AFM. Also, epoxy resin was placed onto a microscope slide. A small amount of epoxy was then transferred to the end of the cantilever by slowly moving the cantilever into the epoxy region. After that, the cantilever with epoxy was used to pick up an Au spherical particle which was previously placed and located on the microscope slide (same microscope slide with the one used for epoxy). The spherical particle strongly adhered to the cantilever after 24 h of curing in room temperature. Also, the probe with a flat-ended tip (probe B) was prepared from contact sliding of a Si probe (AC160, Olympus) on a bare Si substrate to flatten the tip due to wear, as proposed in previous study [35]. The experimental parameters for the flattening process were determined based on the reported wear coefficients of the Si tip [36]. The sliding contact was performed under 9 μN normal force for 20 mm sliding distance on a bare Si substrate. In addition, a probe with an approximately 25-nm-thick metal (PtIr)-coated tip with a nominal radius of 20 nm (ATEC-EFM, Nanosensors) and a probe with a Si tip with a nominal radius of 7 nm (PPP-LFMR, Nanosensors) were used as manufactured (probes C and D, respectively). The nominal normal spring constants or flexural stiffnesses of

probes A, B, C, and D were 42 N/m, 26 N/m, 2.8 N/m, and 0.2 N/m, respectively. The AFM probes with these nominal flexural stiffnesses were selected to apply sufficient forces for measurable indentation during force-indentation curve measurements. The shapes of the tips were carefully characterized using a scanning electron microscopy (SEM) before force-indentation curve measurements. The elastic moduli and Poisson's ratios of Au (78 GPa and 0.42, respectively) [37] and Si (169 GPa and 0.3, respectively) [38] were taken from the literature for probe A, and probes B and D, respectively, to determine elastic moduli of the specimens based on contact models. For probe C, the elastic modulus and Poisson's ratio of PtIr (190 GPa and 0.38, respectively) [39] were used for simplicity, considering that the deformation was expected to occur mainly at the end of the tip.

Three different polymers, polyacrylic acid (PAA, $M_w = 3,000,000$ g/mol), polyvinylidene fluoride (PVDF, $M_w = 180,000$ g/mol), and styrene-butadiene rubber (SBR, $M_w = 430,000$ g/mol) were used as specimens to investigate the effect of friction on the mechanical property measurements from force-indentation data, given that friction-induced hysteresis may be significant for the specimens with low mechanical properties [30]. This was also expected to help minimize the change in the tip shape due to wear. These polymers were deposited onto Cu substrates using an automatic film applicator coater. Distilled water was used as a solvent for PAA and SBR, whereas n-methyl-2-pyrrolidone was used to dissolve PVDF. The solutions were deposited on Cu substrates using an automatic film applicator coater. After deposition, the specimens were dried in a convection oven at 60 °C for 30 min and in a vacuum oven at 80 °C for 24 h to completely remove residual solvent. The thicknesses of the polymer films were about 5 μm . The topographies of the specimens were observed with intermittent contact mode of AFM using a Si probe (AC240, Olympus). Fig. 3.1 shows AFM topography images of the specimens. The semi-crystalline structure

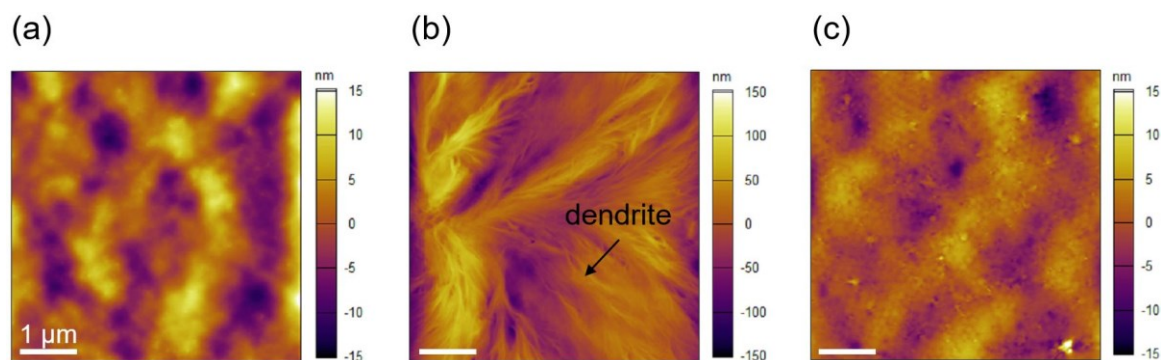


Fig. 3.1. AFM topography images of the (a) PAA, (b) PVDF, and (c) SBR specimens.

represented by a dendrite crystalline phase [40] can be observed for PVDF specimen, while the structures of PAA and SBR specimens are expected to be amorphous. The periodic pattern can also be observed in the topography of the SBR specimen from Fig. 3.1, which may be associated with the ordered lattice structure of the latex surface [41]. The average surface roughnesses of the PAA, PVDF, and SBR specimens were calculated to be 3.9 ± 0.4 , 26 ± 5 , and 2.6 ± 0.3 nm, respectively (mean \pm 1 standard deviation), from the AFM topographic images obtained at five different locations with a $5 \mu\text{m} \times 5 \mu\text{m}$ scanning area. The difference in structures of the specimens may be responsible for the difference in surface roughness values. Poisson's ratios of PAA, PVDF, and SBR specimens taken from literature were used (0.4, 0.36, and 0.5, respectively) for the determination of elastic moduli based on contact models [42-44].

3.1.2 Methods

A commercialized AFM (MFP-3D, Asylum Research, Santa Barbara, CA) was used to obtain force-displacement curves in ambient conditions. Initially, the probes were carefully aligned with the AFM coordinate system to eliminate sliding in lateral direction during force-displacement curve measurements. Force-displacement data was converted

into force-indentation data by subtracting the cantilever deflection calculated using photo-detector output and deflection sensitivity from the displacement measured using a sensor equipped with the AFM. The deflection sensitivity, S_d , was determined from the slopes in more than ten force-displacement curves obtained on a bare Si substrate for each probe. In all force-displacement curves, the deflection sensitivity obtained from the retraction curve, $S_{d,ret}$, was consistently greater than the deflection sensitivity obtained from extension curve, $S_{d,ext}$, as shown in Fig. 3.2. This suggests that the difference between $S_{d,ret}$ and $S_{d,ext}$ is systematic, likely attributed to friction [17-20]. The differences between $S_{d,ret}$ and $S_{d,ext}$ were calculated to be on the scale of 3.9%, 0.7%, 1.1%, and 2.4% for probes A, B, C, and D, respectively. To compensate for this difference, the S_d of the probes was determined by taking the mean of $S_{d,ret}$ and $S_{d,ext}$ [19]. S_d values of probes A, B, C, and D were determined to be 11.7 ± 0.1 V/ μm , 16.7 ± 0.1 V/ μm , 11.6 ± 0.1 V/ μm , and 13.6 ± 0.1 V/ μm , respectively. For probes A and D, the differences between $S_{d,ret}$ and $S_{d,ext}$ were found to be larger by factors of 4 and 5 than statistical uncertainties in S_d , respectively. In contrast, the differences between $S_{d,ret}$ and $S_{d,ext}$ for probes B and C are comparable to the statistical uncertainties of S_d . It can be seen that the uncertainty associated with the friction could be relatively small, but it was often present even in the data obtained from the bare Si surface. Also, the differences can be clearly observed when the cantilever deflection was subtracted from displacement, as shown in Fig. 3.2 (b).

The flexural stiffnesses, k_N , of the probes were obtained from thermal noise method [45] prior to force-indentation curve measurements. k_N values of probes A, B, C, and D were determined to be 44 ± 1 N/m, 46 ± 2 N/m, 2.0 ± 0.1 N/m, and 0.60 ± 0.01 N/m,

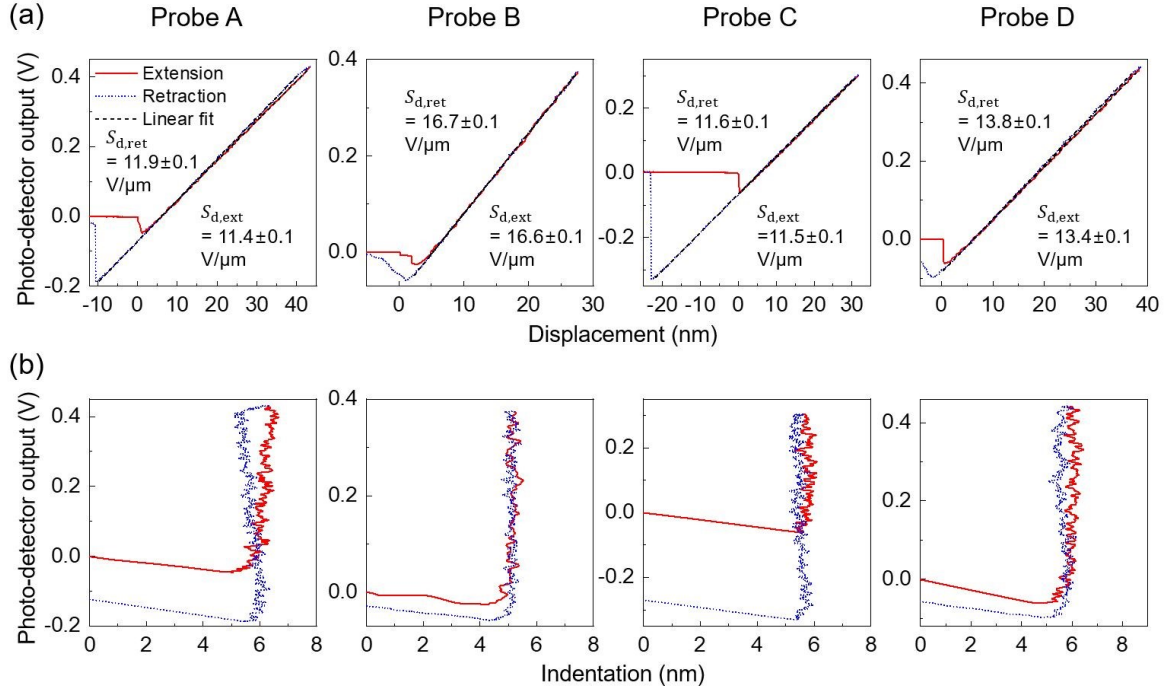


Fig. 3.2. Photo-detector output with respect to (a) displacement and (b) indentation obtained using probes A, B, C, and D against a bare Si substrate. In (b), cantilever deflection was determined using the photo-detector output and mean of deflection sensitivities from extension and retraction curves ($S_{d,ext}$ and $S_{d,ret}$, respectively), and indentation was obtained by subtracting the cantilever deflection from piezo displacement.

respectively, from ten measurements. The maximum normal forces for probes A, B, C, and D were set to be about 1.6 μN , 1 μN , 50 nN, and 20 nN, respectively, so that indentations were measurable using an AFM without plastic deformation. Given that the indentations were a few orders of magnitude smaller than the thickness of the polymer thin films (~ 5 μm), the effect of the substrate on force-indentation data can be neglected. The time-dependent behavior of polymer specimens was outside the scope of this work and, therefore, the speed was kept at a relatively low constant of 100 nm/s to minimize the effect of viscous behavior during force-indentation curve measurements. The entire indentation time was approximately 1 second with a speed of 100 nm/s, which is significantly lower

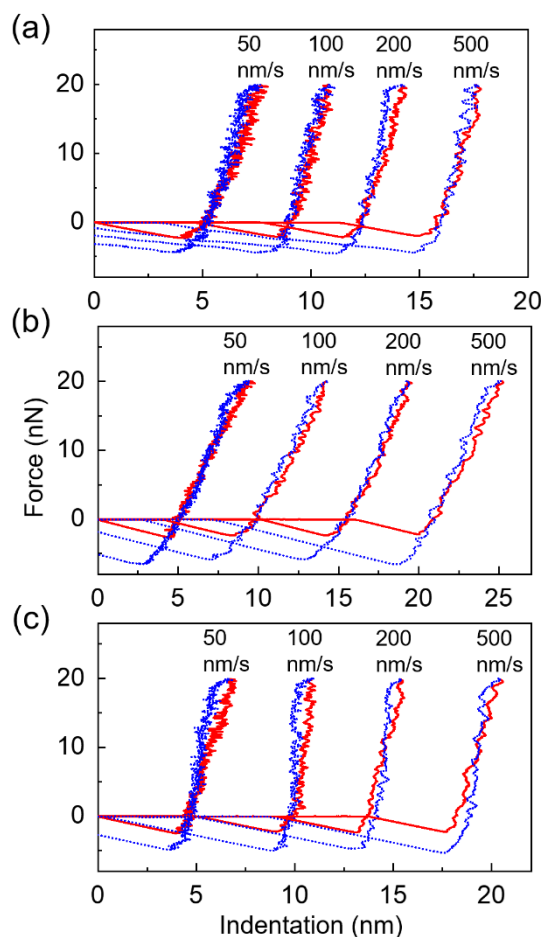


Fig. 3.3. Force-indentation curves of the (a) PAA, (b) PVDF, and (c) SBR specimens obtained at speeds ranging from 50 nm/s to 500 nm/s using probe D.

than the relaxation time of similar types of polymers used in this work [46-48], and therefore the viscoelastic behavior during indentation was likely to be negligible [49]. In addition, no substantial difference in the force-indentation data obtained at various speeds ranging from 50 nm/s to 500 nm/s, as shown in Fig. 3.3. This suggests that viscoelastic behavior of the specimens was not significant for the experimental conditions used in this work.

A total of 64 force-indentation curves were obtained on randomly selected locations with a $5 \mu\text{m} \times 5 \mu\text{m}$ scanning area for each specimen. After the force-indentation curve measurements, AFM images of the indentation locations on the specimens were examined

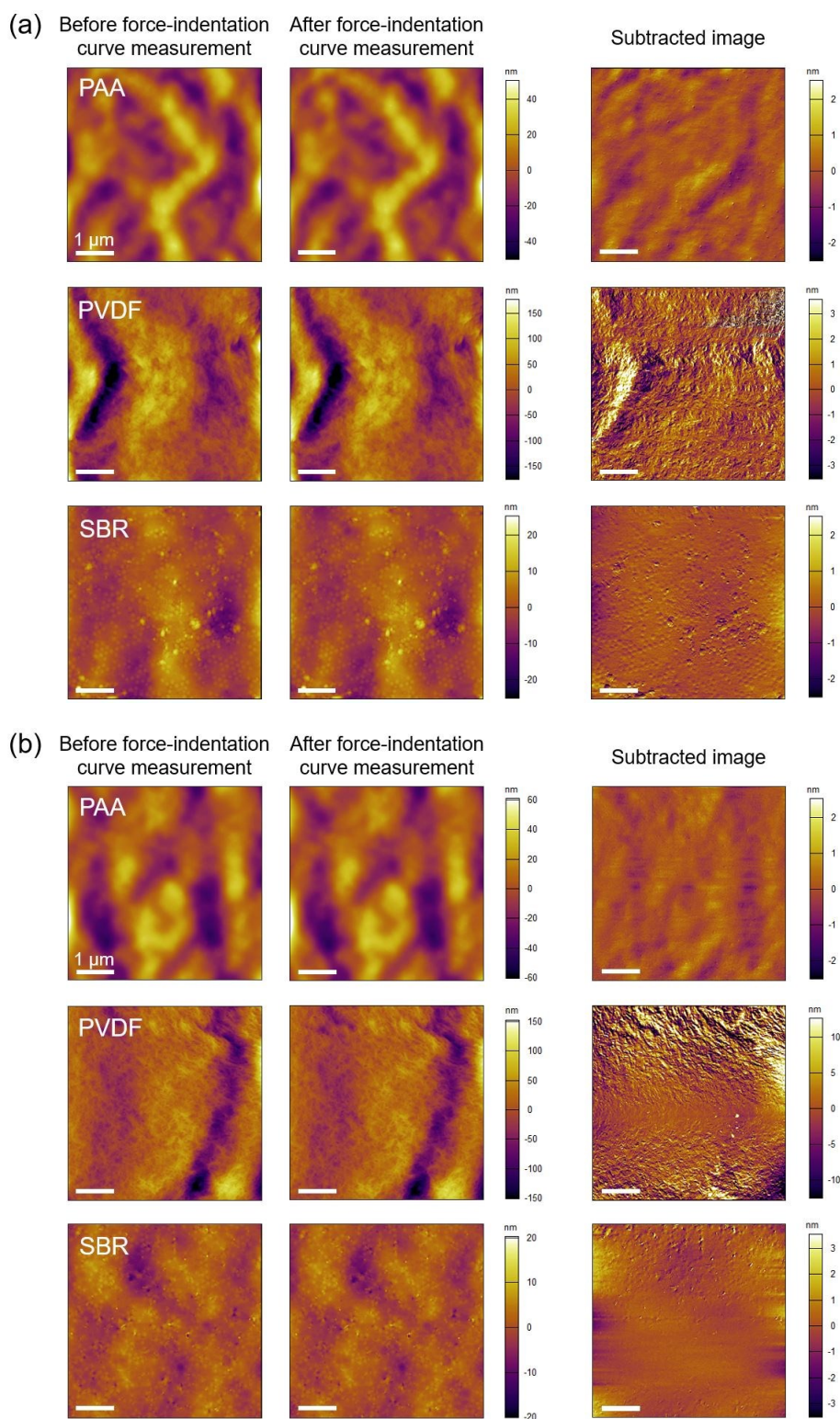


Fig. 3.4. AFM images of the PAA, PVDF, and SBR specimens before and after force-indentation curve measurements using probes (a) C and (b) D. AFM images after the measurements subtracted from those obtained before the measurements were included for comparison.

to determine whether plastic deformation occurred, as can be observed in Fig. 3.4. The data in Fig. 3.4 clearly show that no significant residual deformation was observed on the specimens after force-indentation curve measurements for the cases of probes C and D, where contact pressures were relatively high. Hence, elastic contact between the tips and the specimens during force-indentation curve measurements was assumed. The contact model was carefully selected depending on tip shape, as described in the following section, and the elastic moduli of the specimens were obtained from both extension and retraction curves. In addition, the elastic moduli of the specimens were obtained using instrumented indentation (UNHT³, Anton Paar) for comparison [50,51]. Maximum normal force, loading rate, and holding time were set to be 50 μN , 10 $\mu\text{N}/\text{min}$, and 30 sec, respectively, for the instrumented indentation.

3.2 Probe with spherical tip

Figure 3.5 (a) shows SEM images of probe A. It can be clearly observed from Fig. 3.5 (a) that the Au particle glued on the cantilever was quite spherical. The radius of the tip of probe A was determined to be about of 7.6 μm . Figure 3.5 (b) shows the force-indentation curves obtained from the PAA, PVDF, and SBR specimens using probe A. As shown, the pull-off force is significant for all specimens. Also, as shown in Fig. 3.5 (b), the indentation depths of the specimens ranged from 2.0 nm to 7.4 nm and were significantly smaller than the tip radius of probe A. In this regard, the JKR model was used to calculate elastic modulus from the data obtained using probe A. For a sphere making contact with an elastic substrate, the relationship between the force, F , and the indentation, δ , can be obtained from Eqs. (3.1) and (3.2), based on the JKR model [52].

$$a^3 = \frac{3R}{4E^*} \left(F + 3\gamma\pi R + \sqrt{6\gamma\pi R F + (3\gamma\pi R)^2} \right) \quad (3.1)$$

$$\delta = \frac{a^2}{R} - \sqrt{\frac{2\gamma\pi a}{E^*}} \quad (3.2)$$

where a is the contact radius, R is the tip radius of the probe, E^* is the reduced elastic modulus, and γ is the work of adhesion. E^* can be determined from Eq. (3.3).

$$\frac{1}{E^*} = \frac{1 - \nu_t^2}{E_t} + \frac{1 - \nu_s^2}{E_s} \quad (3.3)$$

where E_t and E_s are the elastic moduli, ν_t and ν_s are the Poisson's ratios of the tip and the specimen, respectively. E^* and γ can be determined from the curve fitting using Eqs. (3.1) and (3.2) [53,54], and then E_s could be obtained using Eq. (3.3). γ can also be obtained separately from the pull-off force using Eq. (3.4), based on the JKR model.

$$F_{\text{pull-off}} = -\frac{3}{2}\gamma\pi R. \quad (3.4)$$

The JKR model fits obtained using Eqs. (3.1) and (3.2) are presented in Fig. 3.5 (b). It can be clearly seen from Fig. 3.5 (b) that differences between the extension and retraction curves were significant for all specimens. Plastic deformation and viscoelastic behavior were not likely to be significant during the force-indentation curve measurements. Also, the displacement was directly measured using a sensor equipped with the AFM and, therefore, effect of hysteresis or creep of the piezo scanner on the force-indentation data was not a significant concern. Thus, it was plausible that the difference between the extension and retraction curves shown in Fig. 3.5 (b) can be mainly attributed to friction. Friction generates a torque that opposes the normal bending moment, which causes underestimation and overestimation of the deflection signal from the photo-detector (y -axis) in the extension and retraction curves, respectively [16-20]. This results in additional overestimation and underestimation of indentation in the extension and retraction curves,

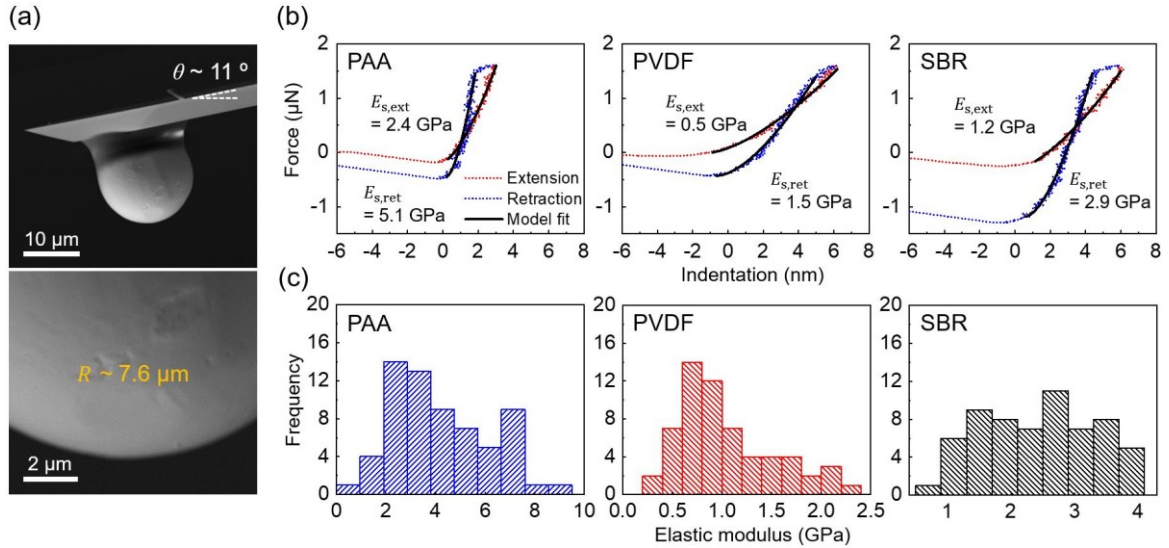


Fig. 3.5. (a) SEM images of probe A, and (b) force-indentation curves, and (c) histograms of mean elastic modulus of the PAA, PVDF, and SBR specimens obtained using probe A.

respectively, when indentation is obtained by subtracting the cantilever deflection from the displacement. Hence, the difference between the extension and retraction curves, attributed to the friction, becomes more significant due to the conversion of force-displacement data into force-indentation data. E_s was approximated by taking the mean of the elastic moduli determined from the extension and retraction curves, $E_{s,\text{ext}}$ and $E_{s,\text{ret}}$, respectively, by assuming that the effect of friction is equal and opposite between the extension and retraction data [19].

Figure 3.5 (b) shows that JKR model fits agreed well with both extension and retraction curves for all specimens. Also, no significant signs of plastic deformation [5] were observed from the figure. From the data shown in Fig. 3.5 (b), $E_{s,\text{ext}}$ and $E_{s,\text{ret}}$ were calculated to be 2.4 GPa and 5.1 GPa, 0.5 GPa and 1.5 GPa, and 1.2 GPa and 2.9 GPa for the PAA, PVDF, and SBR specimens, respectively. As expected, the differences between $E_{s,\text{ext}}$ and $E_{s,\text{ret}}$ were calculated to be about 71%, 97%, and 84% for the PAA, PVDF, and SBR specimens, respectively. Figure 3.5 (c) shows histograms of E_s values determined from 64 force-

indentation curves obtained using probe A, for the PAA, PVDF, and SBR specimens. The averages of E_s values of the PAA, PVDF, and SBR specimens were calculated to be 4.2 ± 2.0 GPa, 1.2 ± 0.7 GPa, and 2.4 ± 1.0 GPa, respectively. a values were estimated to be 190 ± 30 nm, 270 ± 30 nm, and 250 ± 20 nm for the PAA, PVDF, and SBR specimens, respectively. Mean contact pressures for PAA, PVDF, and SBR specimens were calculated to be 15 ± 4 MPa, 7 ± 2 MPa, and 8 ± 1 MPa, respectively, under a normal force of $1.6 \mu\text{N}$.

3.3 Probe with flat ended tip

SEM images of probe B are provided in Fig. 3.6 (a). As shown, the tip of probe B was quite flat with an inclination of about 11° . This inclination was likely due to the probe mounting angle in the AFM system, and it was expected to help achieve better contact between the flat end of the tip and the specimens. Also, the flat end of the tip was quite

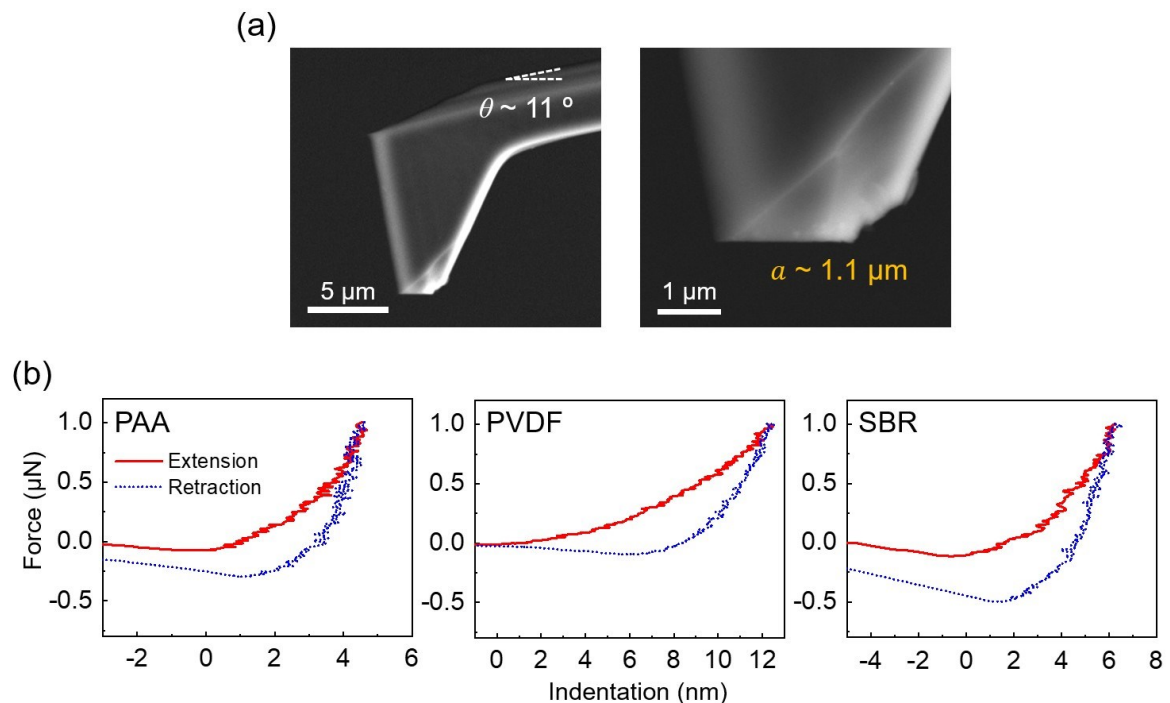


Fig. 3.6. (a) SEM images of probe B, and (b) force-indentation curves of the PAA, PVDF, and SBR specimens obtained using probe B.

clean and no significant wear debris were observed. The radius of the flat end of the tip, which corresponds to a , was determined to be 1.1 μm from the SEM image shown in Fig. 3.6 (a). Figure 3.6 (b) shows force-indentation curves obtained from the PAA, PVDF, and SBR specimens using probe B. For a flat tip making contact with an elastic substrate, the relationship between the force and indentation is expected to be linear [55]. However, it was clearly seen from Fig. 3.6 (b) that the slope increased with increasing indentation. In particular, the increase in slope was gradual at the initial stage of contact. This outcome may be associated with the misalignment between the flat end of the tip and the specimen surface, as observed for instrumented indentation [56], probably due to the specimen surface roughness and misalignment of the probe relative to the AFM coordinate system. The contact area was likely to increase with increasing indentation due to the misalignment, which in turn resulted in an increase in the slope. In addition, it is worthy to note that the misalignment could lead to local plastic deformation of the specimen near the edge of the tip [57]. The data shown in Fig. 3.6 (b) suggests the possible occurrence of plastic deformation although the experiments were carefully performed to eliminate the plastic deformation. Hence, it was difficult to determine E_s values from the force-indentation data presented in Fig. 3.6 (b) using a contact model for a flat tip. This outcome suggests that a probe with a flat tip was not recommended for nanomechanical property measurements of even relatively soft materials with a few nm average surface roughness.

The hysteresis in the force-indentation curves was also found to be more significant for probe B than for probe A, probably due to the misalignment between the flat tip of probe B and the specimen surface. Also, the forms of force-indentation curves obtained using probe B were quite different from those obtained using probe A. It is interesting to note that the hysteresis was more significant for the PVDF specimen than for PAA and SBR

specimens. The larger surface roughness of PVDF may be partly responsible for this outcome. Consequently, it was difficult to address the contribution of friction to hysteresis in force-indentation curves for the case of probe B. The contact pressure calculated using the radius of the flat end of the tip was about 6 MPa under a normal force of 1.0 μN . However, the actual contact pressure was expected to be larger than this value due to the misalignment.

3.4 Probe with conical tips with rounded apices

SEM images of probe C are presented in Fig. 3.7 (a) along with a hyperbolic profile. As can be seen from Fig. 3.7 (a), the hyperbolic profile was found to well represent the tip shape of probe C. For adhesive contact between a hyperboloid and an elastic substrate, the relationship between F and δ can be obtained from Eqs. (3.5) and (3.6) for adhesive contact [27].

$$\delta = \frac{aA}{2R} \left[\frac{\pi}{2} + \arcsin \left(\frac{(a/A)^2 - 1}{(a/A)^2 + 1} \right) \right] - \left(\frac{2a\pi\gamma}{E^*} \right)^{1/2} \quad (3.5)$$

$$F = 2E^* \left[\frac{A}{2R} \left[aA + \frac{a^2 - A^2}{2} \left(\frac{\pi}{2} + \arcsin \left(\frac{(a/A)^2 - 1}{(a/A)^2 + 1} \right) \right) \right] - a \left(\frac{2a\pi\gamma}{E^*} \right)^{1/2} \right] \quad (3.6)$$

In Eqs. (3.5) and (3.6), $A = R \cot(\alpha)$, and α is half of apex angle. For probe C, R and α were determined to be 30 nm and 15° , respectively, from the data shown in Fig. 3.7 (a). E^* and γ also could be determined from curve fitting based on Eqs. (3.5) and (3.6) [27], similar to the JKR model, and then E_s could be determined using Eq. (3.3). It should be noted that the inclination of the tip with respect to the specimen surface, φ , was about 19°

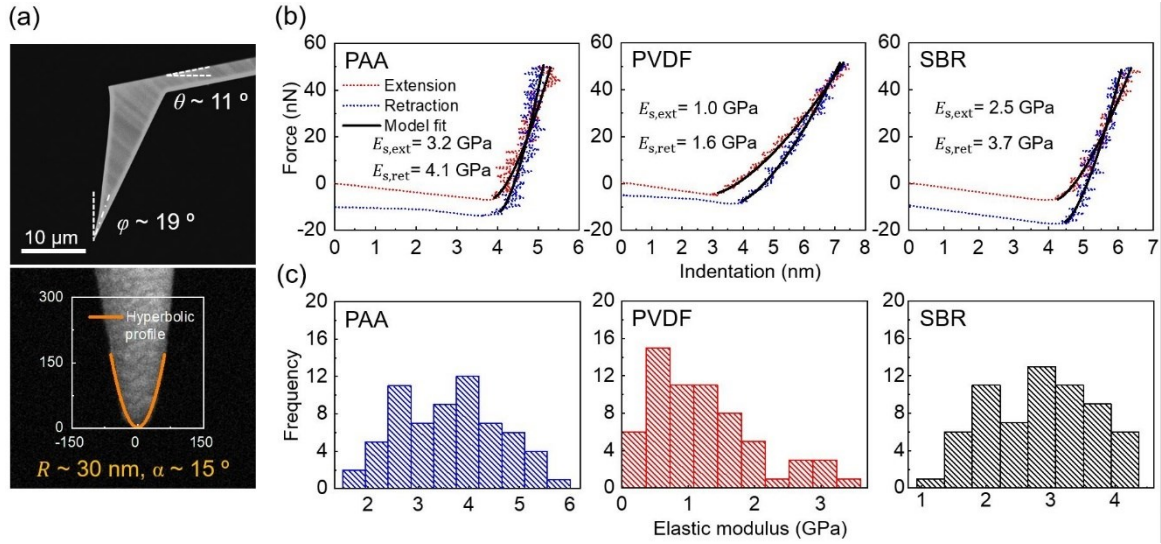


Fig. 3.7. (a) SEM images of probe C, and (b) force-indentation curves, and (c) histograms of mean elastic modulus of the PAA, PVDF, and SBR specimens obtained using probe C.

due to the mounting angle of the probe and inclination of the tip with respect to the cantilever, as shown in Fig. 3.7 (a).

Figure 3.7 (b) shows force-indentation data of the PAA, PVDF, and SBR specimens obtained with probe C and the model fits obtained using Eqs. (3.5) and (3.6). It can be seen from Fig. 3.7 (b) that force-indentation data consistently agreed with the hyperbolic model fits through the entire indentation, without significant signs of plastic deformation [5]. Similar to the case of probe A, significant differences in the extension and retraction curves were also observed in the data obtained using probe C, as shown in Fig. 3.7 (b). $E_{s,ext}$ and $E_{s,ret}$ were calculated to be 3.2 GPa and 4.1 GPa, 1.0 GPa and 1.6 GPa, and 2.5 GPa and 3.7 GPa for the PAA, PVDF, and SBR specimens, respectively, from the data shown in Fig. 3.7 (b). The differences in $E_{s,ext}$ and $E_{s,ret}$ were determined to be about 26%, 45%, and 37% for the PAA, PVDF, and SBR specimens, respectively. Figure 3.7 (c) shows the histograms of E_s determined from 64 force-indentation curves. From the data shown in the figure, the averages of E_s values were calculated to be $3.6 \pm 1.0 \text{ GPa}$, $1.2 \pm 0.8 \text{ GPa}$, and

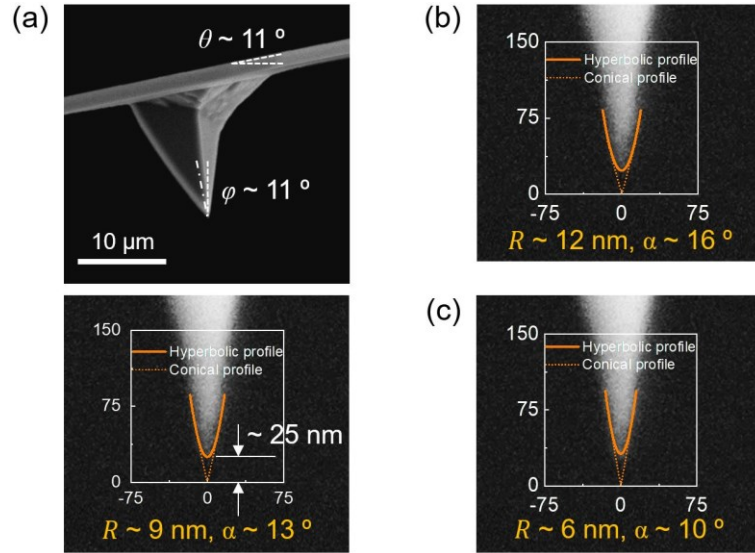


Fig. 3.8. (a) SEM images of probe D and (b) upper and (c) lower bounds of tip radius and half apex angle of probe D determined from the SEM image considering the blurring boundary.

2.8 ± 0.8 GPa for the PAA, PVDF, and SBR specimens, respectively. a was determined to be relatively large (14 ± 1 nm, 18 ± 3 nm, and 14 ± 1 nm for the PAA, PVDF, and SBR specimens, respectively) considering the R of probe C (~ 30 nm), which further indicates that the hyperbolic model was more appropriate than the spherical model [19,54]. The estimated mean contact pressures were about 90 ± 20 MPa, 60 ± 10 MPa, and 80 ± 10 MPa for the PAA, PVDF, and SBR specimens, respectively. The higher contact pressures for probe C were due to a smaller tip radius compared to probe A despite the smaller indentation depths (1.2 nm to 4.3 nm) as shown in Fig. 3.7 (b).

SEM images of probe D along with the hyperbolic profile are shown in Fig. 3.8 (a). The hyperbolic profile well described the conical shape with a round apex of the tip of probe D, similar to that of probe C. However, the uncertainties in R and α were relatively large for probe D compared with probe C due to the limitations of SEM images. Hence, R and α were carefully obtained by considering the upper and lower bounds of R and α , as shown in Figs. 3.8 (b) and 3.8 (c), respectively, determined from a rigorous comparison of

the hyperbolic profile and SEM image. As result, R and α of probe D were determined to be 9 nm and 13° , respectively, as shown in Fig. 3.8 (a). The conical profile is also presented in Fig. 3.8 (a) for comparison. In contrast to the hyperbolic profile, the conical profile did not agree with the tip shape of probe D due to the round apex of the tip. In particular, considering that the distance between the ends of the actual tip and the conical profile was about 25 nm, the conical model should be applied when indentation depth is significantly larger than 25 nm. Since the indentation depth was smaller than 5 nm for probe D, the force-indentation data were interpreted using the hyperbolic model. Also, φ for probe D was determined to be about 11° when it was mounted in the AFM.

Force-indentation curves obtained using probe D and the model fits obtained using Eqs. (3.5) and (3.6) are shown in Fig. 3.9 (a). It should be noted that abnormal force-indentation curves, which are likely to be associated with pinning of the tip [17,18], were often observed for the case of probe D, as shown in Fig. 3.10. The occurrence of pinning

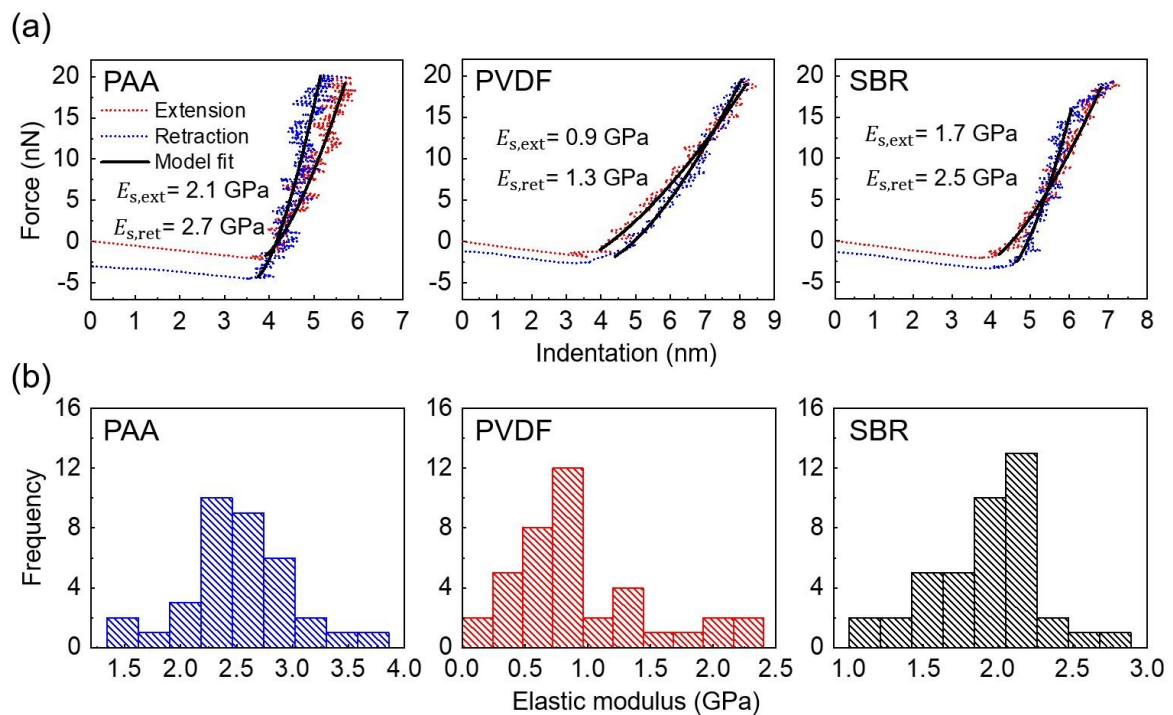


Fig. 3.9. (a) Force-indentation curves and (b) histograms of mean elastic modulus of the PAA, PVDF, and SBR specimens obtained using probe D.

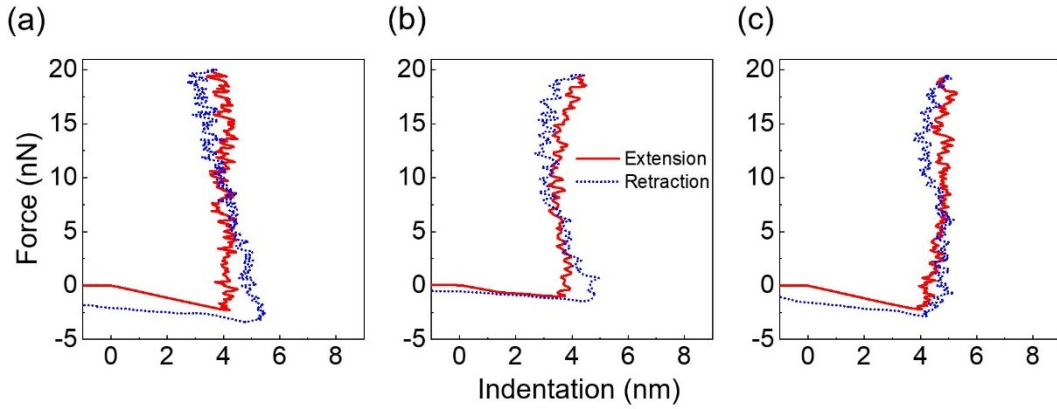


Fig. 3.10. Examples of abnormal force-indentation curves obtained from the (a) PAA, (b) PVDF, and (c) SBR specimens using probe D.

might be associated with adhesion between the tip and specimen, surface roughness of the specimen, and degree of deformation [17]. These force-indentation data were not used in the determination of elastic modulus. From Fig. 3.9 (a), difference between extension and retraction curves were clearly observed for probe D, consistent with the results from probes A and C. From the data shown in Fig. 3.9 (a), $E_{s,ext}$ and $E_{s,ret}$ were calculated to be 2.1 GPa and 2.7 GPa, 0.9 GPa and 1.3 GPa, and 1.7 GPa and 2.5 GPa, which correspond to 25%, 37%, and 36% differences for the PAA, PVDF, and SBR specimens, respectively. Figure 3.9 (b) shows the histograms of E_s values determined from 35, 39, and 41 force-indentation curves obtained using probe D for the PAA, PVDF, and SBR specimens, respectively. The averages of E_s were calculated to be 2.5 ± 0.5 GPa, 0.9 ± 0.5 GPa, and 1.9 ± 0.4 GPa for the PAA, PVDF, and SBR specimens, respectively. a (7 ± 1 nm, 8 ± 1 nm, and 7 ± 1 nm for the PAA, PVDF, and SBR specimens, respectively) was comparable to R of probe D, which suggests that the hyperbolic model was more suitable than the spherical model for more accurate determination of E_s [32,58]. The mean contact pressures (150 ± 30 MPa, 100 ± 20 MPa, and 130 ± 30 MPa for the PAA, PVDF, and SBR specimens, respectively) were calculated to be relatively larger than those obtained using probes A and C, as expected.

3.5 Comparison of measurement results

$E_{s,ext}$, $E_{s,ret}$, and E_s values obtained using probes A, C, and D are summarized in Table 3.1. E_s values determined using the instrumented indentation were also provided in Table 3.1. The results generally showed that E_s values were found to agree with each other within experimental uncertainties for all specimens. Also, the E_s values of the PAA and PVDF specimens obtained from this work were in agreement with those in previous studies [1,2]. The elastic moduli determined from this work for the SBR specimen were greater than the elastic modulus of the bulk [59], which may be associated with differences in fabrication method and conditions, and dependence on the measurement scale, as is often observed in literature [60]. Examples of force-indentation curves from the instrumented indentation are shown in Fig. 3.11. The E_s values of PAA, PVDF, and SBR specimens determined using the instrumented indentation were 5 ± 2 GPa, 1.7 ± 0.7 GPa, and 3.3 ± 0.7 GPa, respectively. E_s obtained from instrumented indentation were slightly larger values than those obtained using the AFM, likely attributed to the differences in measurement scale and conditions. However, the E_s values obtained from the AFM and the instrumented indentation was found to generally agree with each other within experimental uncertainty. As shown in Table 3.1, E_s measurement results exhibited large deviations, as generally observed for polymers [1,2,24]. A plausible explanation of this result is local variation in the elastic properties due to disorder in the amorphous structure of the polymer. As for the PVDF specimen with a semi-crystalline structure, the difference in elastic properties between crystalline and amorphous phases may also be responsible for large data scattering. Nevertheless, comparison of E_s values suggests that the effect of friction can be compensated for by taking the mean of $E_{s,ext}$ and $E_{s,ret}$.

Table 3.1 Summary of the elastic moduli determined for the PAA, PVDF, and SBR specimens.

Specimen	AFM									Instrumented indentation
	Probe A			Probe C			Probe D			In air
	$E_{s,ext}$ (GPa)	Difference ^a	E_s (GPa)	$E_{s,ext}$ (GPa)	Difference ^a	E_s (GPa)	$E_{s,ext}$ (GPa)	Difference ^a	E_s (GPa)	E_s (GPa)
$E_{s,ret}$ (GPa)	(%)		$E_{s,ret}$ (GPa)	(%)		$E_{s,ret}$ (GPa)	(%)			
PAA	2.7 ± 1.6	70	4.2 ± 2.0	3.3 ± 1.0	22	3.6 ± 1.0	2.2 ± 0.5	26	2.5 ± 0.5	5 ± 2
	5.7 ± 2.7			4.0 ± 1.1			2.9 ± 0.5			
PVDF	0.6 ± 0.3	100	1.2 ± 0.7	1.0 ± 0.6	42	1.2 ± 0.8	0.7 ± 0.4	43	0.9 ± 0.5	1.7 ± 0.7
	1.8 ± 1.3			1.5 ± 1.0			1.1 ± 0.6			
SBR	1.4 ± 0.7	81	2.4 ± 1.0	2.4 ± 0.7	32	2.8 ± 0.8	1.6 ± 0.3	33	1.9 ± 0.4	3.3 ± 0.7
	3.4 ± 1.4			3.3 ± 1.0			2.2 ± 0.5			

^a Difference between elastic moduli calculated from the extension and retraction curves was determined using the equation $\frac{(E_{s,ret} - E_{s,ext}) \times 100\%}{E_s}$.

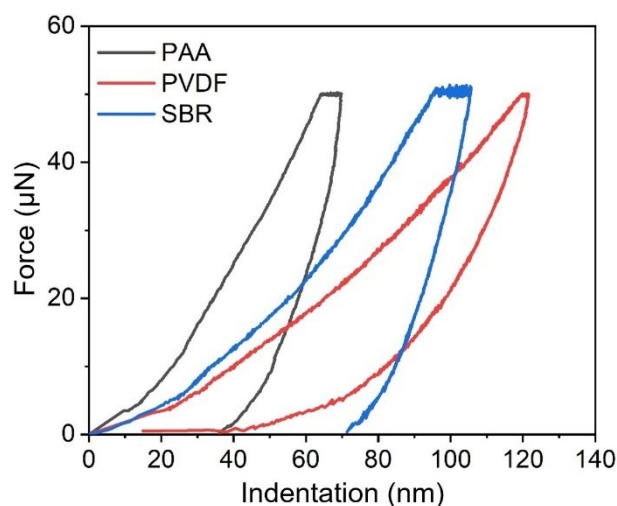


Fig. 3.11. Force-indentation curves of the PAA, PVDF, and SBR specimens obtained from instrumented indentation.

The use of the probe with a large tip radius is helpful to apply a large force and indentation under a low contact pressure. Hence, using the probe with a large tip radius decreases the probability of plastic deformation and reduces uncertainties associated with force and displacement measurements using an AFM. To compare the relative uncertainty in the displacement measurement, residuals between actual indentation data and model fits were normalized by indentation depth, as shown in Fig. 3.12. It can be seen from the figure that fluctuations in the data were significantly smaller for probe A than for probes C and D. This indicates that the precision of indentation data obtained using probe A was greater than the data obtained using probes C and D. In addition, the contact pressures estimated from contact models were smaller for probe A than for probes C and D, as expected, which is preferred for minimization of plastic deformation due to high stress. It should also be noted that commercialized AFM probes often have an inclination in the tip to specimen surface (ϕ), as shown in Figs. 3.7 (a) and 3.8 (a). Since the tip with a large radius can be modeled as a sphere for relatively large indentation depths, uncertainty associated with this tip inclination can be reduced, while the uncertainty in indentation measurement is

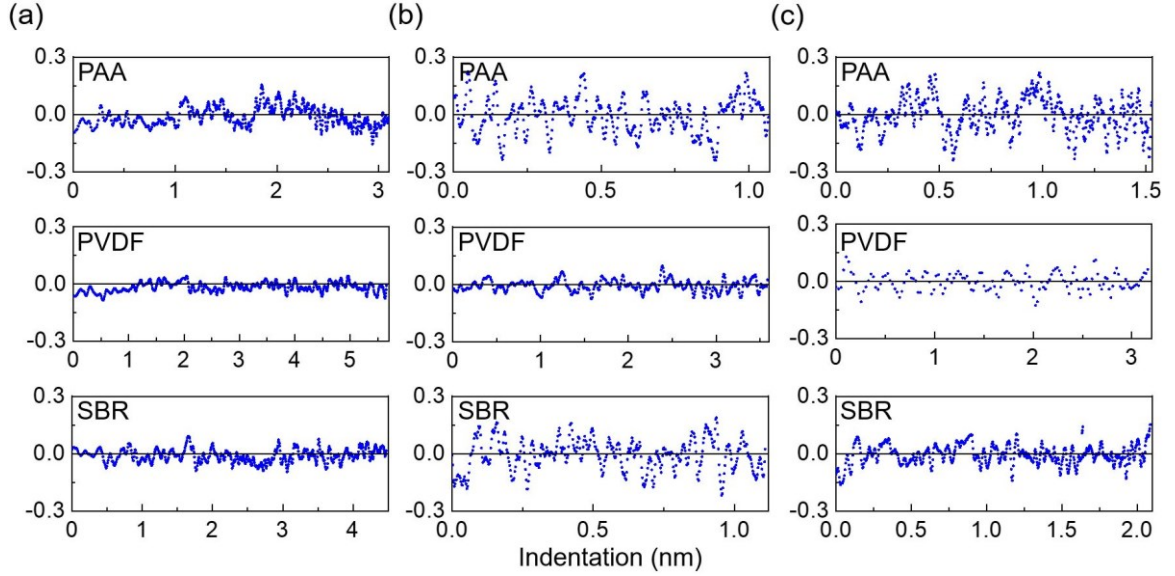


Fig. 3.12. Residuals between indentation data and model fits normalized by the indentation depth for probes (a) A, (b) C, and (c) D.

maintained. Furthermore, the tip with a large radius may plausibly exhibit lower wear progression during force-indentation curve measurements [33,34]. Another advantage of the probe with the large tip radius is the relatively small uncertainty in tip characterization, as can be seen Figs. 3.5 (a) and 3.7 (a). In contrast, the probe with smaller tip radius is preferred for the measurement of elastic modulus with high lateral resolution. It is worthy noting that the estimated contact radii from contact models were orders of magnitude larger for probe A than probes C and D. Hence, probe A is not recommended for mechanical property measurements with high lateral resolution. Thus, a probe with a tip radius of a few tens of nanometers could be recommended to map elastic modulus associated with surface microstructures for the specimen with a few GPa elastic modulus.

The hysteresis in force-displacement curves due to friction can depend on the flexural stiffnesses of the AFM probe and specimen [20]. To investigate the effects of the stiffnesses of the AFM probe and specimen, the ratio $E_{s,ret}/E_{s,ext}$ is plotted as a function of the ratio k_{con}/k_N , where $k_{con} = 2aE^*$ is the contact stiffness obtained from the contact model at

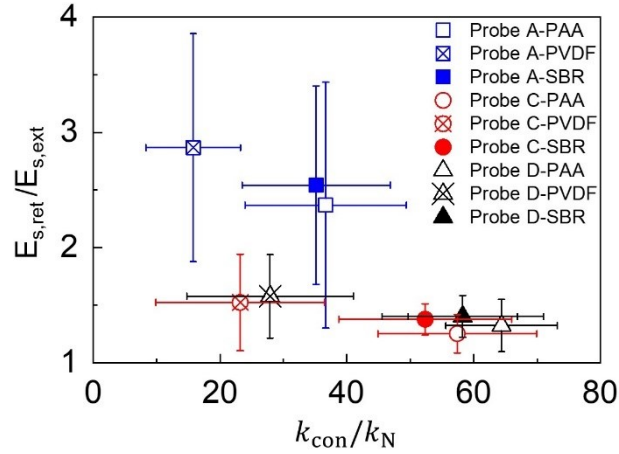


Fig. 3.13. Ratio of elastic moduli of the specimens determined from the extension and retraction curves, $E_{s,ret}/E_{s,ext}$, as a function of the ratio of contact stiffness to flexural stiffness of probes, k_{con}/k_N .

the maximum normal force, as shown in Fig. 3.13. It should be noted that the contact stiffness generally increases due to increase in contact radius as normal force increases. Therefore k_{con} should be considered as the upper bound of contact stiffness. The friction characteristics between tip and specimen, and tip height can further determine the friction-induced torque, and therefore it can affect $E_{s,ret}/E_{s,ext}$, as well [17,18,20]. However, as shown in Fig. 3.14, the friction loop measurement results showed that friction characteristics of the specimens sliding against a given tip were quite similar to each other and that the tip heights of probes A, C, and D were quite similar to each other. Figure 3.13 shows that $E_{s,ret}/E_{s,ext}$ generally decreased as k_{con}/k_N increased for each probe, which is consistent with previous study [20]. This indicates that the difference between $E_{s,ext}$ and $E_{s,ret}$ may be more significant for softer specimens. It can also be seen from the figure that $E_{s,ret}/E_{s,ext}$ was generally larger for probe A than probes C, and D. Probably, relatively large friction between the tip of probe A and the specimens (associated with a large adhesion force due to the large tip radius) may be responsible for this outcome. In addition, the decrease in $E_{s,ret}/E_{s,ext}$ with increasing k_{con}/k_N was found to be relatively small for

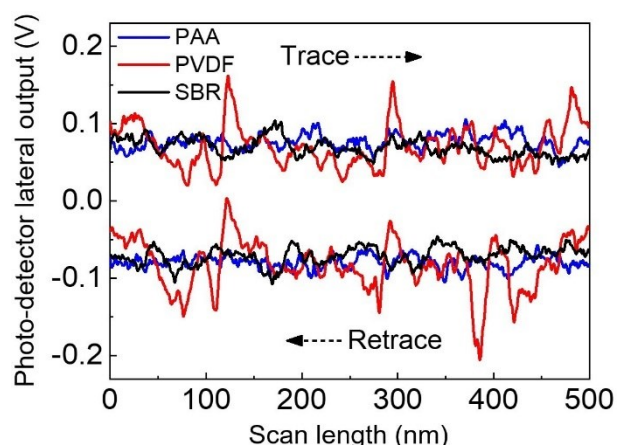


Fig. 3.14. Examples of friction loops of the PAA, PVDF, and SBR specimens slid against a Si probe under a 10 nN normal force.

probe A, compared to probes C and D. These outcomes suggest that probe A may not be preferred for the specimens used in this work. In this regard, probes for elastic modulus measurements should be carefully selected to minimize the hysteresis associated with friction, particularly for soft materials with high friction characteristics. For example, contact stiffness can readily increase with increasing tip radius due to increase in contact radius and, therefore, a probe with a large tip radius may be preferred. However, the probe with a larger tip radius can exhibit larger adhesion, which in turn could cause an increase in friction. In addition, for a probe with a large tip radius, the relatively large normal force should be applied for sufficient indentation depth and, therefore, the probe should have a large flexural stiffness. Hence, a probe with a minimal flexural stiffness is recommended as long as it can apply sufficient force.

The results suggest that hysteresis due to friction should be avoided or minimized as much as possible for accurate determination of elastic modulus from a force-indentation curve obtained using an AFM. Also, it should be noted that the adhesive contact model without friction was used for the interpretation of force-indentation data, due to a lack of an adhesive contact model that consider friction. This in turn can cause systematic

uncertainty in the elastic modulus due to frictional energy dissipation. In addition, the effects of contact conditions (e.g., inclination of tip to specimen surface) on the occurrence of hysteresis should be systematically investigated. In this regard, theoretical approaches are needed to compensate for the effect of friction on force-indentation data in future work. Furthermore, the effect of tip shape on nanomechanical properties measurements, associated with the friction effect, should be investigated more rigorously using specimens with a wide range of mechanical and frictional properties. Nevertheless, the outcomes may be useful for probe selection and for a better understanding of force-indentation data regarding friction-induced hysteresis, which may be useful for more accurate nanomechanical property measurements using an AFM.

3.6 Summary

In this chapter, force-indentation data were obtained using four different AFM probes with spherical and flat-ended tips, and conical tips with rounded apexes. The data were interpreted to determine the elastic moduli of the specimens based on the adhesive contact models. PAA, PVDF, and SBR specimens were used as specimens. The probe with a flat ended tip was prone to misalignment even with the specimen with a few nm of surface roughness and, therefore, it could not measure the elastic moduli of the specimens. The probes with the spherical tip and conical tips with rounded apexes, which could be modeled as spherical and hyperbolic, respectively, exhibited a significant difference between the extension and retraction curves, plausibly associated with the friction between the tip and the specimen. The difference between extension and retraction curves was found to further propagate during conversion from force-displacement data to force-indentation data. As a result, the difference between the elastic moduli of the specimens determined from

extension and retraction curves was as large as 22 – 100%. The elastic modulus of the specimen was approximated by taking mean values between the elastic moduli from extension and retraction curves. This elastic modulus was found to generally agree with those from instrumented indentation. In addition, although the elastic moduli obtained using the probes with spherical tip and conical tips with rounded apexes agreed with each other within experimental uncertainties, the probe with a relatively large tip radius (e.g., ~ 30 nm) was recommended for mechanical property measurement of the specimens used in this work (i.e., specimens with a few GPa elastic moduli), considering the uncertainties associated with tip characterization, and force and indentation measurements. Furthermore, it was shown that the difference between elastic moduli determined from extension and retraction curves became significant when the ratio of contact stiffness to flexural stiffness of the AFM probe decreased. The outcome is expected to provide useful information for accurate mechanical property measurements using an AFM.

Chapter 4 Nanomechanical properties measurements of polymer binders for lithium-ion batteries

4.1 Introduction and objectives

Si has been proposed as a potential candidate for anode material in LIBs due to the high theoretical specific capacity [61]. However, the Si anodes exhibit a large volume expansion and contraction during the lithiation and delithiation processes (i.e., charge and discharge processes) of LIBs [62]. The stress induced by volume change can degrade the mechanical integrity of the anode, which in turn leads to anode fracture and delamination [63]. Such degradation may also affect the electrical contact of Si particles with conducting additives, leading to drastic capacity fading of LIBs. Polymer binder is used to maintain the mechanical integrity of the anode by sustaining the contact between Si particles, conductive additives, and current collector during lithiation and delithiation processes, leading to enhanced cycling stability of LIBs. Also, polymer binders with enhanced mechanical properties are desirable to further improve the mechanical integrity and, thus, increase the electrochemical stability of electrodes for LIBs [1,2,64-66].

Extensive efforts (e.g., cross-linking [64], heat treatment [65], and functionalization [66]) have been made to improve the mechanical properties of polymer binders to enhance the mechanical integrity of electrodes for LIBs. In addition, given that the electrolyte solution is a constituent component of LIBs, the effects of electrolyte on material properties of polymer binders have been also investigated. Previous studies have shown that the mechanical properties of polymers can be significantly altered by immersion in electrolyte solution compared to those in dry states due to swelling of the polymers in electrolyte [67,68]. However, the effects of electrolyte on the mechanical properties of polymer

binders may vary significantly depending on types of polymer and electrolyte solution [1,2,68]. Hence, for proper implementation of polymers as a binder for LIBs, the effects of electrolyte on the mechanical properties of polymer binders should be systematically investigated across a wide spectrum of polymer binders and electrolytes. In particular, considering that Si particles with a size of a few tens of nm have often been used in anodes for LIBs [1,69], assessment of the nanomechanical properties of polymer binders is needed for better insight into the interactions between polymer binder and electrode components such as Si particles, conductive additives, and current collector.

In addition to the mechanical properties, the adhesion property of a polymer binder may also play a critical role since sufficient binding strength between polymer binder and electrode components is needed to maintain contact during the lithiation and delithiation processes of LIBs. It has been demonstrated that polymer binders with improved initial adhesion result in prolonged cycling stability of LIBs [70,71]. It was also shown that adhesion of polymer binders decreases after they contact electrolyte and during the charge and discharge processes [69,72]. In this regard, adhesion should be considered a crucial property of polymer binders, and further quantitative assessment of adhesion is needed for appropriate selection of polymer binders for LIBs.

AFM has been widely used to measure the nanomechanical and adhesion properties of polymer binders [1,2,73,74]. For example, the nanomechanical and adhesion properties of a target specimen can be determined from force-indentation data based on contact models. For accurate measurement of the elastic modulus and intrinsic adhesion properties, the AFM probe tip should be carefully characterized. A colloidal probe can provide a controlled geometry [30] and, therefore, contribute to minimize the uncertainty associated with tip characterization. Also, the colloidal probe can provide relatively large force and indentation

in elastic region during force-indentation curve measurement to justify calculation using the contact model. As a result, uncertainties in the measurements of force and displacement can be reduced [5,13]. In particular, a colloidal probe may be preferred for measurement of the elastic modulus of soft materials since a relatively low contact pressure can be applied under a given force, which is expected to be helpful in observation of electrolyte-induced reduction in the mechanical properties of polymer binders. The uncertainty associated with wear progression of the probe tip [33,34] is likely to be negligible for a colloidal probe. Furthermore, given that the effect of friction on force-indentation data was more clearly observed using the colloidal probe (chapter 3), in this chapter, use of the colloid tip is expected to provide useful information about the friction effect in different environments (e.g., in air and electrolyte).

In this chapter, the nanomechanical and adhesion properties of five different polymer binders were quantitatively assessed using colloidal probe AFM. In particular, the effects of electrolyte on surface and mechanical properties of polymer binders were experimentally investigated. The effect of friction on force-indentation curve measurement is also discussed. Furthermore, work of adhesion of polymer binders was quantitatively assessed based on the contact model. For the specimens, polyacrylic acid (PAA), polyacrylonitrile (PAN), polyvinyl alcohol (PVA), and carboxymethyl cellulose (CMC) were used because they are potential binder candidates in LIBs. A conventional binder, polyvinylidene fluoride (PVDF), was also evaluated. In addition, the reduced elastic moduli of the specimens were compared with capacity retention of LIBs to understand the relationship between mechanical properties of polymer binders and electrochemical performance of LIBs. The results present in this chapter can be useful to gain a better understanding of the nanomechanical and adhesion properties of various polymer binders for LIBs and,

therefore, provide useful information for selection of polymer binders. Furthermore, the approaches used in this chapter are expected to result in accurate measurements of the nanomechanical properties of soft materials.

4.2 Experimental details

4.2.1 Materials

In this chapter, four different polymers, PAA ($M_w = 3,000,000$ g/mol), PAN ($M_w = 150,000$ g/mol), CMC ($M_w = 150,000$ g/mol), and high molecular weight PVA, were selected considering their potential applicability as a binder for LIBs. Also, high molecular weight PVDF ($M_w = 1,000,000$ g/mol), which is conventionally used as a polymer binder in LIBs, was evaluated. The substitution degree of the CMC used in this work was about 1. Also, PVA was prepared with a degree of saponification of 94%, given that it showed enhanced cycling stability [69]. The molecular weights of the CMC and PVDF used in this work were comparable to those of commercial CMC and PVDF used as binders in LIBs. Also, the PAA, PAN, and PVA with relatively high molecular weights were selected, given that a high molecular weight polymer may be preferred for improved mechanical property and strong adhesion. The deposition process of polymers on Cu substrates is as aforementioned (section 3.1.1). In brief, distilled water was used as a solvent for PAA, PVA, and CMC, whereas n-methyl-2-pyrrolidone was used to dissolve PAN and PVDF. After deposition on Cu substrates using an automatic film applicator coater, the specimens were dried in a convection oven at 60 °C for 30 min and in a vacuum oven at 80 °C for 24 h. The thicknesses of the polymer films were about 5 μm . The electrolyte solution used in this work was composed of 1 M LiPF₆ dissolved in 1:1:1 ethylene carbonate:dimethyl

carbonate:ethyl methyl carbonate by volume, which is similar to conventional electrolytes used in LIBs.

Colloidal probes were prepared for force-indentation curve measurements. Details of the procedure for preparing the colloidal probe are given in section 3.1.1. Briefly, Au spherical particle was glued onto the tip-less probe with a nominal normal spring constant of 42 N/m (TL-NCH, Nanosensors). Also, a colloidal probe prepared using an AFM probe with a nominal normal spring constant of 2 N/m (AC240, Olympus) was used for force-indentation curve measurements of PVDF specimen in electrolyte, given that the elastic modulus of PVDF in electrolyte was remarkably small. The radii of the Au spherical particles ranged from 7 μm to 9 μm . The radius of Au spherical particles and the normal spring constant of the probe were carefully selected to apply sufficient normal forces to result in large enough indentation depths within the elastic region during force-indentation curve measurements, such that the uncertainties of the force and displacement using AFM can be reduced [5,13].

4.2.2 Methods

AFM measurements were performed using a commercial AFM (MFP-3D, Asylum Research). After measurements were performed under ambient conditions (23-25 $^{\circ}\text{C}$, 35-40 % relative humidity), the specimens were immersed in electrolyte for 12 h. Then, the specimens were allowed to equilibrate for 2 h in electrolyte using a closed fluid cell before data was collected to minimize the uncertainties associated with thermal drift of AFM [75]. A total of 64 force-displacement curves were obtained using the colloidal probes at randomly selected locations over a 5 μm \times 5 μm scan area for each specimen in air and in

electrolyte. The force-displacement data were converted into force-indentation data by subtracting cantilever deflection from displacement. Then, the spherical contact model was used to obtain the reduced elastic moduli for the specimens. The reduced elastic moduli were calculated using both extension and retraction curves of the force-indentation data, given that friction could cause hysteresis in force-indentation data [16-20]. To understand the effects of electrolyte on the surface structures of the polymer binders, topographic images were obtained in air and in electrolyte in intermittent contact mode using a Si probe (AC240, Olympus). The root-mean-square surface roughness, R_q , was also obtained from AFM topographic data obtained at five locations with a scan area of $5 \mu\text{m} \times 5 \mu\text{m}$.

Displacement was measured using a sensor equipped as part of the AFM. Also, for quantitative force measurement, normal force calibration was performed based on the thermal noise method [45] prior to force-indentation curve measurements. The deflection sensitivity, S_d , in air was determined from more than 10 force-displacement curves obtained from a bare Si substrate under ambient conditions. Particularly, S_d was determined from the average slopes of extension and retraction curves in the force-displacement data to minimize the uncertainty associated with friction [19]. The S_d values of the colloidal probes prepared using TL-NCH and AC240 were calculated to be $16.5 \pm 0.1 \text{ V}/\mu\text{m}$ and $17.5 \pm 0.1 \text{ V}/\mu\text{m}$, respectively, in air. The normal spring constant values, k_N , of the colloidal probes prepared using TL-NCH and AC240 were determined to be $51 \pm 2 \text{ N/m}$ and $1.34 \pm 0.05 \text{ N/m}$, respectively, from 10 thermal noise spectra obtained in air. Since the location of the laser spot on the probe should be readjusted for measurement in electrolyte, the value of S_d in electrolyte was separately determined from force-displacement curves obtained on a bare Si substrate in electrolyte. Similar to the S_d determination in air, S_d in electrolyte was determined from the mean slopes of the

extension and retraction curves. However, the effect of friction on force-displacement data was found to be negligible in electrolyte. The S_d values of the colloidal probes prepared using TL-NCH and AC240 were determined to be 12.1 ± 0.1 V/ μm and 21.3 ± 0.1 V/ μm , respectively, in electrolyte. It should be noted that S_d can also be obtained from a simple harmonic oscillator model using a thermal noise spectrum obtained in electrolyte when the spring constant is known [76]. The S_d values of the colloidal probes prepared using TL-NCH and AC240 were calculated to be 13.8 ± 0.3 V/ μm and 21.2 ± 0.1 V/ μm , respectively, from 10 thermal noise spectra obtained in electrolyte. The difference between the S_d values determined from the force-displacement curve and thermal noise spectra in electrolyte was as large as 13%. It is likely that the S_d value determined from the force-displacement curve is more accurate than that obtained from the thermal noise spectrum, considering the uncertainties associated with the correction factor in estimation of S_d from the thermal noise spectrum [77,78]. However, this result also suggests that the S_d value estimated from the thermal noise spectrum in electrolyte can be used, depending on allowed uncertainty in the normal force measurement, for cases where the tip should be protected from contact before an experiment.

Normal forces up to 1.6 μN were applied during the force-indentation curve measurements in air. However, the maximum normal force was set to 0.9 μN for the PAA, PAN, PVA, and CMC specimens and to 24 nN for the PVDF specimen during force-indentation curve measurements in electrolyte. These maximum normal force values were determined to obtain a relatively large indentation depth within the elastic region, depending on the specimens. Since the time-dependent behavior of polymer specimens is not within the scope of this work, the speed was kept constant at 100 nm/s to minimize the effect of the viscous contribution during force-indentation curve measurements. The total

time for each force-indentation curve measurement was about 1 second, which is significantly faster than the relaxation time of similar types of polymers used in this work [46,47,79-81]. As a result, the viscoelastic behavior during indentation is likely to be negligible [49].

To clearly understand the effect of friction on force-indentation data [16-20], friction loops were also obtained in air and in electrolyte. The friction loops of the specimens were obtained using a Si probe with a nominal normal spring constant of 0.2 N/m (PPP-LFMR, Nanosensors). The k_N value of the probe used for friction loop measurement was determined to be 0.16 ± 0.01 N/m using the thermal noise method [45]. For friction loop measurement, lateral force calibration was separately performed in air and in electrolyte based on the improved wedge method under various normal forces [82,83]. The lateral force sensitivity, S_L , of the probe used for friction loop measurements was 7.31 mV/nN in air and 10.17 mV/nN in electrolyte. More than 8 friction loops were obtained at different locations on each specimen, with a normal force of 10 nN and a sliding speed of 300 nm/s.

The reduced elastic moduli of the specimens were determined from instrumented indentation (UNHT³, Anton Paar) for comparison. The instrumented indentation was performed with a maximum normal force of 500 μ N, a loading rate of 100 μ N/min, and a holding time of 60 sec, at up to 10 different locations of the specimens. Then, the reduced elastic moduli of the specimens were obtained from force-indentation data based on the Oliver-Pharr method [50].

4.3 Surface structures

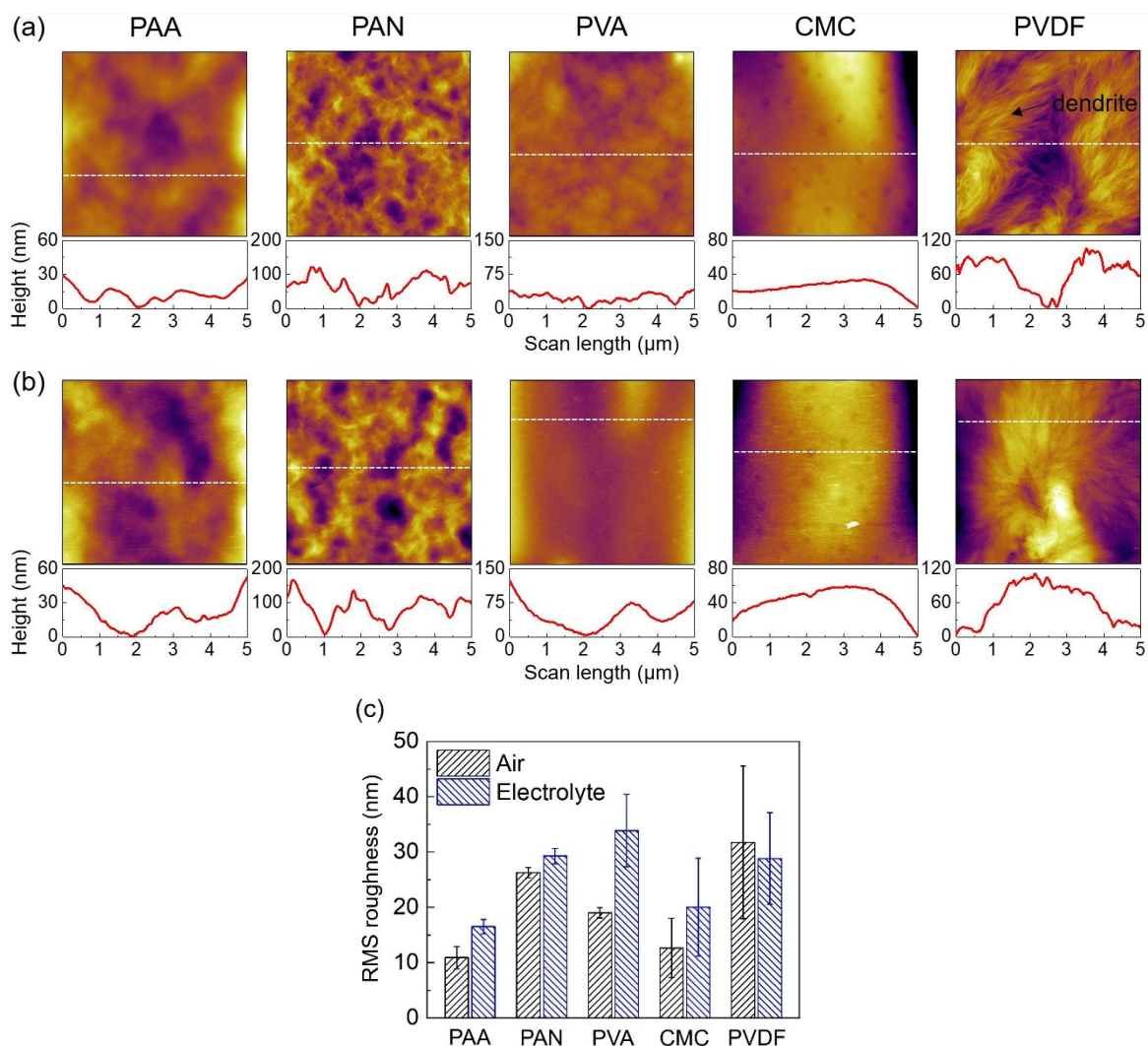


Fig. 4.1. AFM images of the PAA, PAN, PVA, CMC, and PVDF specimens obtained in (a) air and (b) electrolyte, and (c) RMS surface roughnesses of the specimens in air and electrolyte.

Figure 4.1 (a) shows topography images of the specimens obtained in air along with the cross-sectional height profiles of the specimens. The topography images and cross-sectional height profiles show that the surface structures of the specimens were different. The semi-crystalline structure represented by a dendrite crystalline phase was observed for PVDF specimen, while PAA, PAN, PVA, and CMC specimens were expected to have an

amorphous structure. Interestingly, small pits that likely formed during the fabrication process were found on the surface of the CMC specimen, as shown in Fig. 4.1 (a). To understand the effects of electrolyte on the surface structures of specimens, topographic images of the specimens were also obtained in electrolyte, as shown in Fig. 4.1 (b). In general, the surface structures of the PAA, PAN, CMC, and PVDF specimens were not significantly altered due to immersion in electrolyte, as can be determined from Figs. 4.1 (a) and (b). However, a difference in surface structures of the PVA specimens in air and in electrolyte was observed.

The R_q values of the specimens in air and in electrolyte are summarized in Fig. 4.1 (c), which shows that the surface roughness increased for the PAA, PAN, PVA, and CMC specimens and slightly decreased for the PVDF specimen. The R_q values of the PAA, PAN, PVA, CMC, and PVDF specimens in air were calculated to be 11 ± 2 nm, 26 ± 1 nm, 19 ± 1 nm, 13 ± 5 nm, and 32 ± 14 nm, respectively. The R_q values of the PAA, PAN, PVA, CMC, and PVDF specimens in electrolyte were determined to be 17 ± 1 nm, 29 ± 1 nm, 32 ± 5 nm, 20 ± 9 nm, and 29 ± 8 nm, respectively. The increases in R_q values of the PAA, PAN, PVA, and CMC specimens in electrolyte were calculated to be 55%, 12%, 68%, and 54%, respectively, compared to those in air. The increases in surface roughness can be attributed to swelling of the amorphous polymer in electrolyte [84-86]. Also, the more significant increase in surface roughness of PVA may be associated with the change in surface structure observed in Figs. 4.1 (a) and (b). In contrast to the PAA, PAN, PVA, and CMC specimens, the R_q value of the PVDF specimen in electrolyte was found to be 9% smaller than in air. The different effects of electrolyte on the surface roughness may originate from the dependence of the swelling behavior on the polymer structure (e.g., amorphous and crystalline) [85,87,88]. For a semi-crystalline polymer such as PVDF,

diffusion of solvent molecules from electrolyte into the polymer structure may cause unfolding and subsequent disentanglement of polymer chains in the crystalline phase. Therefore, a gradual transition from crystalline to amorphous phase can occur [87,88], resulting in a decrease in surface roughness [89]. Hence, the increase in surface roughness in electrolyte can feasibly be cancelled out due to the crystalline-to-amorphous phase transition. It is worthy to note that polymer binders with an amorphous structure can provide enhanced cycling performance, given that an amorphous polymer may provide more uniform coverage for the Si particles [90]. In addition, a polymer binder with a low surface roughness can be preferred to increase the surface coverage between the polymer binder and electrode components, which may further contribute to enhanced adhesion. In this regard, the PAA and CMC specimens with relatively low surface roughness in electrolyte may be advantageous.

4.4 Nanomechanical and adhesion properties

4.4.1 Measurement results in air

Figure 4.2 (a) shows the force-indentation curves obtained for the PAA, PAN, PVA, CMC, and PVDF specimens in air. As can be seen from the figure, a significant difference between extension and retraction curves was observed for all specimens. No significant sign of plastic deformation was observed in the extension and retraction curves [5]. Also, the viscoelastic behavior was likely to be negligible for the conditions employed in this work. In addition, hysteresis from the piezo-actuator was not likely to be significant, given that the displacement was measured using a sensor equipped as part of the AFM during force-indentation curve measurements. Therefore, it was likely that the difference between

the extension and retraction curves was mainly due to friction, as mentioned in the previous chapter. Assuming that the effect of friction is equal and opposite between the extension and retraction data [19], the reduced elastic modulus for the specimen was approximated using the mean elastic moduli obtained from the extension and retraction curves.

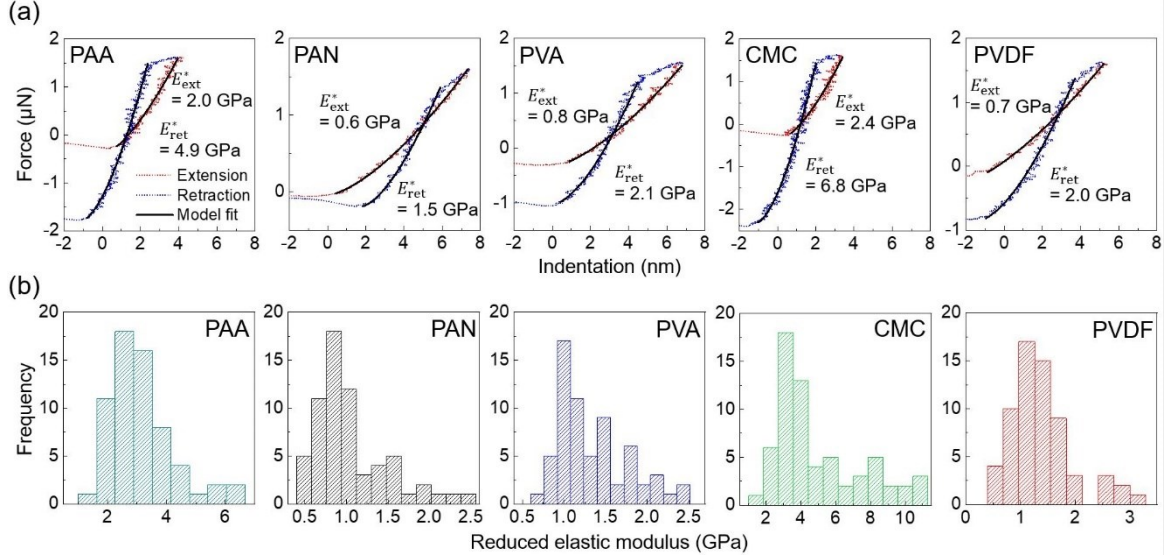


Fig. 4.2. (a) Force-indentation curves and (b) histograms of the means of reduced elastic moduli determined from extension and retraction curves for the PAA, PAN, PVA, CMC, and PVDF specimens in air.

From the data shown in Fig. 4.2 (a), the pull-off force was found to be significant for all specimens. Also, the indentation depths of the specimens ranged from 2.5 nm to 6.8 nm for the given measurement conditions, which is significantly smaller than the tip radius of the colloid probe. Therefore, to interpret the data, the use of an adhesive contact model for the spherical tip is justified. In this regard, the JKR model was used to analyze the force-indentation data obtained in air. Also, since the elastic modulus of Au was significantly larger than that of the polymer specimens used, E^* can be approximated using Eq (4.1).

$$\frac{1}{E^*} \approx \frac{1 - \nu_s^2}{E_s}. \quad (4.1)$$

From the fit results shown in Fig. 4.2 (a), it can be seen that the JKR model fits agreed with the force-indentation data for all specimens. The reduced elastic moduli determined from the extension and retraction curves, E_{ext}^* and E_{ret}^* , were calculated to be 2.0 GPa and 4.9 GPa, 0.6 GPa and 1.5 GPa, 0.8 GPa and 2.1 GPa, 2.4 GPa and 6.8 GPa, and 0.7 GPa and 2.0 GPa for the PAA, PAN, PVA, CMC, and PVDF specimens, respectively, using the data shown in Fig. 4.2 (a). The differences between E_{ext}^* and E_{ret}^* were calculated to be about 82%, 81%, 87%, 95%, and 94% for the PAA, PAN, PVA, CMC, and PVDF specimens, respectively. Figure 4.2 (b) shows the histograms of E^* approximated as the mean of E_{ext}^* and E_{ret}^* from 64 force-indentation curves of the PAA, PAN, PVA, CMC, and PVDF specimens. The average E^* values were calculated to be 3.3 ± 1.3 GPa, 1.1 ± 0.4 GPa, 1.4 ± 0.4 GPa, 5.0 ± 2.5 GPa, and 1.4 ± 0.6 GPa for the PAA, PAN, PVA, CMC, and PVDF specimens, respectively. The mean contact pressures under maximum normal force were calculated to be 7 ± 1 MPa, 7 ± 1 MPa, 6 ± 1 MPa, 8 ± 3 MPa, and 6 ± 1 MPa for the PAA, PAN, PVA, CMC, and PVDF specimens, respectively. The low values of contact pressure suggest that plastic deformation was not likely during force-indentation curve measurements.

As mentioned in the previous chapter (section 3.2), γ can be obtained from curve fitting and from the pull-off force based on the JKR model. The γ values of the specimens obtained from 64 extension and retraction curves using curve fitting are summarized in Fig. 4.3. Also, the values of γ determined from the pull-off forces are included in Fig. 4.3 for comparison. The average values of γ determined from extension curve fits were 34 ± 25 mJ/m², 2 ± 1 mJ/m², 7 ± 5 mJ/m², 58 ± 24 mJ/m², and 6 ± 4 mJ/m² for the PAA, PAN, PVA, CMC, and PVDF specimens, respectively. Also, the average values of γ obtained from retraction curve fits were calculated to be 53 ± 26 mJ/m², 6 ± 3 mJ/m², 19 ± 10 mJ/m²,

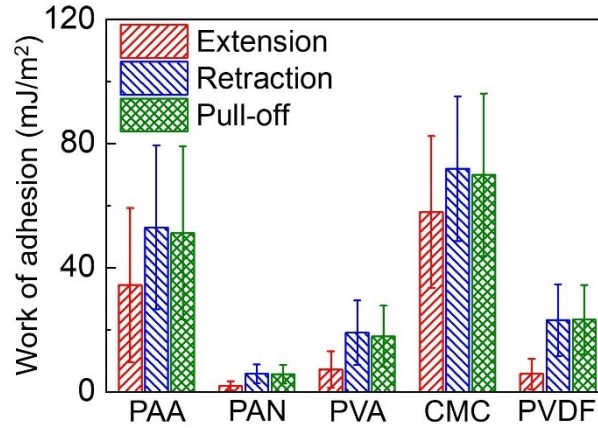


Fig. 4.3. Works of adhesion of the PAA, PAN, PVA, CMC, and PVDF specimens determined from extension and retraction curve fits (E_s^* and γ are unknown parameters for curve fitting) and from the pull-off forces (Eq. (3.4)) based on the JKR model.

$72 \pm 23 \text{ mJ/m}^2$, and $23 \pm 12 \text{ mJ/m}^2$ for the PAA, PAN, PVA, CMC, and PVDF specimens, respectively. The γ values obtained from the retraction curve fits were generally larger than those obtained from the extension curve fits, as expected. The intrinsic mechanical and chemical irreversibility in adhesion and decohesion processes may be responsible for the difference [50,53]. The γ values determined from the retraction curve fits were found to be in agreement with those obtained from the pull-off force, as is often observed for polymers [53,91]. From the data shown in Fig. 4.3, the PAA and CMC specimens exhibited relatively greater work of adhesion compared to the PAN, PVA, and PVDF specimens. This suggests that the PAA and CMC specimens can feasibly provide stronger adhesion properties, which may be helpful for use as a polymer binder [69].

4.4.2 Measurement results in electrolyte

Figure 4.4 (a) shows the force-indentation curves obtained for the PAA, PAN, PVA, CMC, and PVDF specimens in electrolyte. As can be clearly seen from Fig. 4.4 (a), the

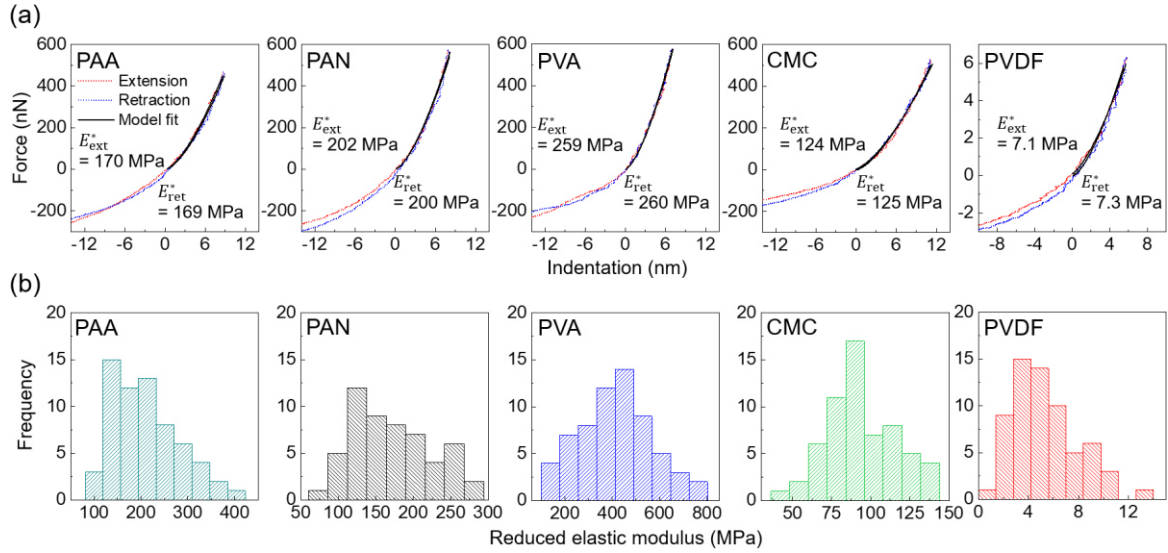


Fig. 4.4. (a) Force-indentation curves and (b) histograms of the means of reduced elastic moduli determined from extension and retraction curves for the PAA, PAN, PVA, CMC, and PVDF specimens in electrolyte.

shapes of the force-indentation curves obtained in electrolyte significantly differed from those obtained in air. The slopes of the force curves gradually increased with increasing indentation and determination of the contact point was not straightforward. This outcome may be associated with the effect of repulsive interaction between the colloidal probe and specimen in electrolyte [92-95]. In addition, the adhesive interaction was likely eliminated by the repulsive interaction in electrolyte, and thus the pull-off force was not clearly observed for all specimens, as shown in Fig. 4.4 (a). Furthermore, in contrast to the force-indentation curves in air, no significant hysteresis was observed for the force-indentation curves in electrolyte, which suggests that the effect of friction on force-indentation data is negligible.

Since no significant adhesion was observed and the indentation depths of specimens were substantially smaller than the tip radius, as shown in Fig. 4.4 (a), the Hertzian model [96] was used to obtain the reduced elastic moduli for the specimens in electrolyte. The

relationship between F and δ can be obtained from Eq. (4.2), based on the Hertzian contact model.

$$F = \frac{4}{3} E^* R^{1/2} \delta^{3/2}. \quad (4.2)$$

As aforementioned, determination of the contact point was not straightforward as a result of being associated with the effect of repulsive interaction in electrolyte. Hence, similar to previous studies [93,94], the contact point was determined as the onset of the compliance slope described by the Hertzian contact model, as shown in Fig. 4.4 (a). The curve fit was performed by increasing the offset from the maximum indentation depth until a significant discrepancy between the experimental data and model fit was observed. The data in Fig. 4.4 (a) show that the extension and retraction curves were in good agreement for all specimens, which suggests that elastic contact occurred during force-distance curve measurement [5]. Histograms of the E^* values determined from 64 force-indentation curves are shown in Fig. 4.4 (b). The averages of E^* were calculated to be 210 ± 70 MPa, 220 ± 130 MPa, 410 ± 150 MPa, 140 ± 50 MPa, and 5.4 ± 2.6 MPa for the PAA, PAN, PVA, CMC, and PVDF specimens, respectively. The mean contact pressures were calculated to be 3 ± 1 MPa, 3 ± 1 MPa, 5 ± 1 MPa, 3 ± 1 MPa, and 0.08 ± 0.03 MPa for the PAA, PAN, PVA, CMC, and PVDF specimens, respectively.

4.4.3 Effect of electrolyte

Table 4.1 shows the summary of reduced elastic moduli determined for specimens in air and electrolyte using colloid probe AFM. As can be seen in Table 4.1, the differences between the E_{ext}^* and E_{ret}^* values in air were significant for all specimens and were calculated to be as large as 73–104%. However, the E_{ext}^* and E_{ret}^* values of all specimens

in electrolyte agreed with each other within experimental uncertainty. These results suggest a significant difference in frictional behaviors of specimens in air and in electrolyte. To clearly understand the difference in frictional behaviors, the friction loops were obtained, as shown in Fig. 4.5. Figures 4.5 (a-e) show the friction loops of the specimens sliding against the Si probe under a 10 nN normal force in air and in electrolyte. The friction forces of the specimens under the given conditions are summarized for comparison in Fig. 4.5 (f). The data shown in Fig. 4.5 clearly demonstrate that friction was significantly smaller in electrolyte compared to in air. The friction force under a 10 nN normal force decreased by 66%, 73%, 81%, 41%, and 53% for the PAA, PAN, PVA, CMC, and PVDF specimens. The decrease in friction could be due to decreases in mechanical properties and adhesion force, which in turn cause a reduction in interfacial shear strength, as is often observed in the friction of polymer in liquid [97,98]. As friction between the tip and specimen decreases, hysteresis in the force-indentation curve weakens due to decrease in torque opposite the normal bending moment during extension and retraction curve measurements. Therefore, the difference between E_{ext}^* and E_{ret}^* values decreases with decreasing friction.

Table 4.1 Summary of the reduced elastic moduli determined for the PAA, PAN, PVA, CMC, and PVDF specimens.

Specimen	AFM						Instrumented indentation
	In air			In electrolyte			In air
	E_{ext}^* (GPa) E_{ret}^* (GPa)	Difference ^a (%)	E^* (GPa)	E_{ext}^* (MPa) E_{ret}^* (MPa)	Difference ^a (%)	E^* (MPa)	E^* (GPa)
PAA	1.9 ± 0.5	82	3.3 ± 1.3	206 ± 70	3	210 ± 70	3.8 ± 0.8
	4.6 ± 2.2			212 ± 70			
PAN	0.7 ± 0.3	73	1.1 ± 0.4	217 ± 130	3	220 ± 130	2.1 ± 0.6
	1.5 ± 0.6			223 ± 130			
PVA	0.8 ± 0.2	79	1.4 ± 0.4	408 ± 150	1	410 ± 150	2.2 ± 1.1
	1.9 ± 0.7			413 ± 150			
CMC	2.4 ± 1.0	104	5.0 ± 2.5	138 ± 50	1	140 ± 50	4.5 ± 1.5
	7.6 ± 4.4			140 ± 50			
PVDF	0.8 ± 0.3	86	1.4 ± 0.6	5.0 ± 2.6	15	5.4 ± 2.6	1.5 ± 0.4
	2.0 ± 0.9			5.8 ± 2.8			

^a Difference between elastic moduli calculated from the extension and retraction curves was determined using the equation $\frac{(E_{\text{ret}}^* - E_{\text{ext}}^*) \times 100\%}{E^*}$.

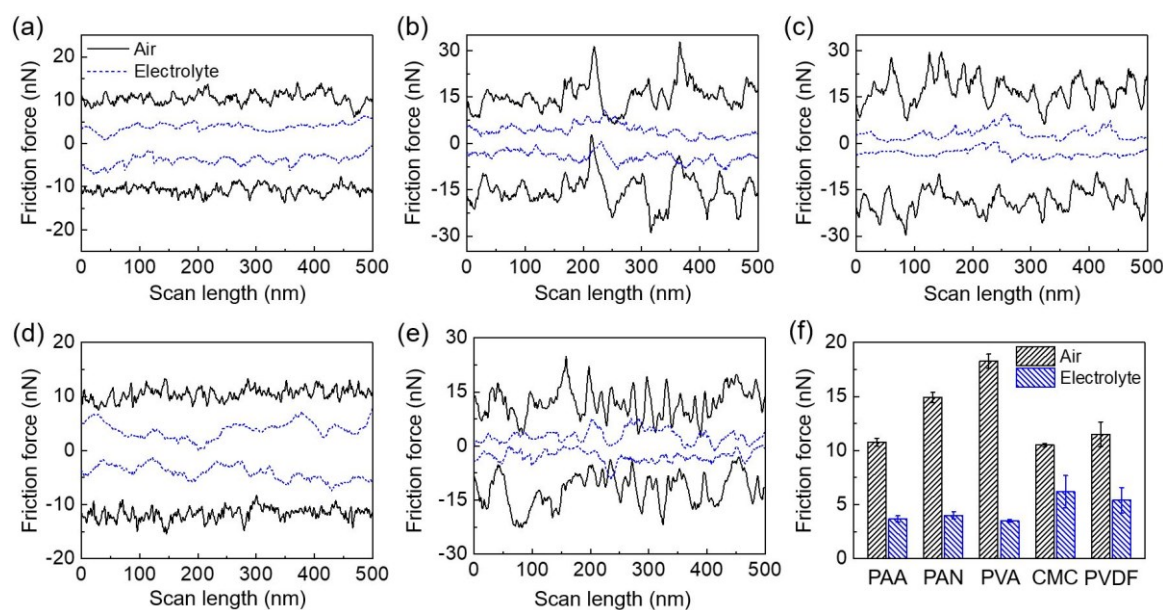


Fig. 4.5. Friction loops of the (a) PAA, (b) PAN, (c) PVA, (d) CMC, and (e) PVDF specimens, and (f) summary of the friction force of the specimen obtained under a 10 nN normal force in air and electrolyte.

Figure 4.6 shows examples of force-indentation curves obtained from the instrumented indentation. The reduced elastic modulus values of the specimens determined using the instrumented indentation were provided in Table 4.1 for comparison. The reduced elastic moduli of the PAA, PAN, PVA, CMC, and PVDF specimens from the instrumented indentation (3.8 ± 0.8 GPa, 2.1 ± 0.6 GPa, 2.2 ± 1.1 GPa, 4.5 ± 1.5 GPa, and 1.5 ± 0.4 GPa, respectively) agreed with those from the AFM within experimental uncertainties. In general, the reduced elastic moduli determined for the specimens in air was also found to agree with those obtained from the literature [1,2,99,100]. In addition, the reduced elastic modulus for the PVDF specimen in electrolyte determined in this work agreed with results of previous studies [5,6]. However, the reduced elastic moduli for the PAA and CMC specimens in electrolyte determined in this work were smaller than those in the literature [1,2]. It is not surprising that the elastic properties of the specimens varied substantially in electrolyte, given that many factors such as fabrication method and conditions, molecular

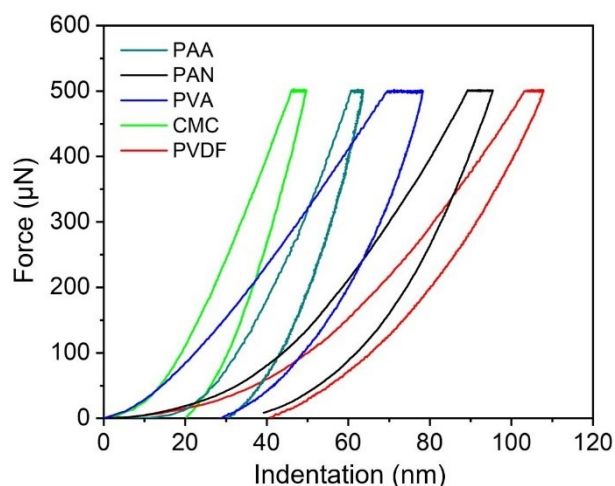


Fig. 4.6. Examples of force-indentation curves of the PAA, PAN, PVA, CMC, and PVDF specimens obtained using instrumented indentation.

weight of polymer, type of electrolyte solution, and immersion time in electrolyte can readily affect polymer swelling [67,68,101,102]. The values reported for elastic moduli of the PAN and PVA specimens in electrolyte are the first of which we are aware. The experimental results showed that the reduced elastic moduli for PAA, PAN, PVA, CMC, and PVDF in electrolyte decreased by factors of 16, 5, 3, 36, and 259, respectively, compared to those in air. Diffusion of solvent molecules from the electrolyte solution into the polymer structure during swelling may increase the mean distance and reduce the cohesive interactions between polymer chains, which lead to decreased mechanical properties in electrolyte [103]. Interestingly, the PAA and CMC specimens exhibited relatively larger reduced elastic moduli than the other specimens in air, while the reduced elastic modulus for PVA was the largest in electrolyte. It should also be noted that decrease in the reduced elastic modulus in electrolyte was most significant for the PVDF specimen compared to the other specimens. This outcome may be associated with the crystalline-to-amorphous phase transition of PVDF in electrolyte, given that crystalline phase often exhibits a higher elastic modulus than the amorphous phase. Also, the polar-polar

interactions among functional groups in PAA, PAN, PVA, and CMC (i.e., carboxyl in PAA, nitrile in PAN, hydroxyl in PVA, and carboxyl and hydroxyl in CMC) may suppress the interaction between the polymer and the electrolyte, which leads to relatively small swelling. This may also be responsible for less decrease in the elastic moduli of PAA, PAN, PVA, and CMC specimens in electrolyte, compared to the PVDF specimen [1,2]. It is worthy to note that the molecular weight of polymer binder feasibly affects not only mechanical properties but also resistance to changes in mechanical properties [101]. However, it was difficult to explore these molecular weight effects using the specimens used in this work.

To understand the relationship between mechanical properties of polymer binders and electrochemical performance of LIBs, the capacity retentions of Si anodes containing PAA, PAN, PVA, CMC, and PVDF binders were compared with E^* values of specimens obtained in electrolyte, as shown in Fig. 4.7. The capacity retentions were estimated based on results reported in previous studies [69,104]. Capacity retentions for Si anodes

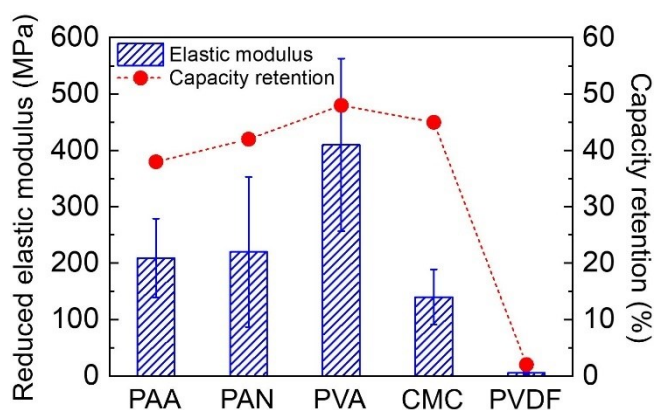


Fig. 4.7. The capacity retention of Si anodes containing PAA, PAN, PVA, CMC, and PVDF binders after 50 charge/discharge cycles along with the reduced elastic moduli of the specimens in electrolyte. The capacity retention is defined as percentage ratio of the capacity after 50 charge/discharge cycles to the initial capacity.

containing PAA, PAN, PVA, CMC, and PVDF after 50 charge/discharge cycles were 38%, 42%, 48%, 45%, and 2%, respectively. As shown in Fig. 4.7, high capacity retention was observed for PAA, PAN, PVA, and CMC specimens, associated with their large E^* values, whereas PVDF exhibited fast capacity fading. The changes in mechanical properties of polymer binders were found to well correlate with the cycling performance of the Si anodes in LIBs, suggesting that understanding of mechanical properties of polymer binder in electrolyte is of importance to develop polymer binders for enhanced mechanical integrity of the electrode. Considering that a relatively large elastic moduli in electrolyte may be preferred for better electrochemical performance, the overall results suggest that the PAA, PAN, PVA, and CMC specimens may be more advantageous than PVDF, as observed in previous studies [1,2,105].

It should be noted that the relationship between the mechanical properties of the polymer binder and the electrode performance should be more systematically investigated to develop a polymer binder with higher electrochemical stability for improved cycling performance [1,2]. Also, to gain better insight into the effects of electrolyte on the mechanical properties of the polymer binder, the effect of immersion time on the mechanical properties of the polymer binder needs to be explored for various types of electrolyte solutions, given that polymer swelling is a time- and solvent-dependent process [68,85,87,88,102]. The effect of molecular weight on resistance to change in the mechanical property of polymer binder in electrolyte needs to be clearly understood [101]. Particularly, the frictional behaviors between the polymer binder and electrode components need to be clearly understood given that the sliding and shearing between the polymer binder and anode components may occur during volume expansion and contraction. Furthermore, better understanding of the adhesion properties between polymer binder and

electrode components in electrolyte may be needed [74]. Nevertheless, the experimental data presented in this work is expected to contribute to understanding of the effect of electrolyte on the mechanical properties of polymer binders and to provide useful information in the design of polymers as binders for enhanced electrochemical stability of electrodes for LIBs. In addition, the approach used in this chapter may be helpful for quantitative measurement of mechanical properties at the nano-scale.

4.5 Summary

In this chapter, the nanomechanical properties of polymer binders of PAA, PAN, PVA, CMC, and PVDF were assessed in air and in electrolyte using AFM. To achieve controlled contact geometry with higher accuracy in force and displacement measurements, force-indentation curves were obtained using colloidal probes. Force-indentation data were also interpreted using contact models to determine the reduced elastic moduli for the specimens. Significant hysteresis was observed in the force-indentation curves obtained in air, and the difference between elastic moduli determined from extension and retraction curves was as large as 73–104%, feasibly due to the effect of friction. However, the effect of friction on force-indentation curves obtained in electrolyte was negligible and can be associated with the significant decrease in friction characteristics of the specimens. The outcomes suggest that understanding of the friction characteristics of the system may be helpful to minimize or avoid the friction-induced hysteresis in force-indentation curves for more accurate measurement of the mechanical properties. The reduced elastic moduli approximated from the mean of reduced elastic moduli from extension and retraction curves for the PAA, PAN, PVA, CMC, and PVDF specimens were 3.3 ± 1.3 GPa, 1.1 ± 0.4 GPa, 1.4 ± 0.4 GPa, 5.0 ± 2.5 GPa, and 1.4 ± 0.6 GPa, respectively. The reduced elastic moduli after immersion in

electrolyte for about 14 h were determined to be 210 ± 70 MPa, 220 ± 130 MPa, 410 ± 150 MPa, 140 ± 50 MPa, and 5.4 ± 2.6 MPa for the PAA, PAN, PVA, CMC, and PVDF specimens, respectively. The reduced elastic moduli in electrolyte were smaller by factors of 3–259 than those in air, likely because of swelling of polymer in electrolyte. It was also found that the effect of electrolyte on the surface roughness may be dependent on the structure of the polymer specimens. In addition, the adhesion properties of the specimens were assessed from the extension and retraction curves and from pull-off forces. The results suggest that PAA, PAN, PVA, and CMC may be more advantageous than PVDF in terms of mechanical properties. Furthermore, PAA and CMC can be more suitable for enhanced adhesion properties based on their lower surface roughness and greater work of adhesion. The outcomes in this chapter may be helpful to gain better understanding of the electrolyte on material properties of polymer binders and, therefore, be helpful to develop polymer binders for improved electrochemical stability of electrodes for LIBs. Furthermore, the approaches used in this chapter can be useful for accurate measurement of mechanical properties of soft materials at the nano-scale.

Chapter 5 Nanomechanical properties measurements of individual collagen fibrils and collagen matrices

5.1 Introduction and objectives

Collagen is one of the most abundant protein in human body that can be found in bones, muscles, skin, blood vessels, and connective tissues [106-108]. Matrices of collagen facilitate the cell behaviors such as proliferation, differentiation, and migration by using their topographical, biochemical, and mechanical cues [109,110]. For example, it has been reported that the mechanical properties of collagen matrices can be increased due to dehydration, leading to increases of cell spreading and proliferation [3,111]. It was also found that dehydration affect the topography of collagen matrices, which may affect cell behaviors [3]. In addition, the lateral stiffness of collagen matrices also plays an important role in cell sensing of the extracellular matrix (ECM) [112]. These results suggest that understanding of the mechanical properties of collagen is crucial in regulating the cell behaviors.

Type I collagen is the dominant structural protein of the ECM which form fibrillar networks that provides strength, elasticity, and mechanical stability to the tissues [108]. In addition, the individual fibril width, length, stiffness, and matrix network structures of collagen I can be tailored into customized patterns, depending on the expected characteristics of cell culture platform. In this regard, matrices of collagen type I have been widely used in cell studies and cancer diagnostics [3,110,112-117]. For example, in human breast cancer, the third tumor-associated collagen signature can be identified through bundles of straightened and aligned collagen around the tumor [115-117]. The mechanical properties of collagen fibrils were also found to increase with progressive stage of cancer

[117]. To mimic the cancer pathological environment, it is of importance to find control the structures of collagen fibrils into bundles.

Previous studies [110,113,114] have found that change in temperature during polymerization process can regulate the formation of collagen fibrils into bundles. Also, optimizations of pH and ionic strength during polymerization were found to play important roles in bundle formation [118,119]. However, the conventional methods to regulate bundle formation from collagen fibrils often require a relatively long polymerization time (e.g., 4 h to 16 h) [110,114], which may be limited for application of the method in 3-dimensional cell culture since long polymerization time can cause cell death. In this chapter, a new method for regulating the structure of collagen matrix network at the nano-scale level is proposed. Bundle structure of collagen network is achieved by incorporating the sulfate anion during the polymerization process of collagen. The proposed method required relatively short polymerization time (about 30 min), which may be helpful to extent application of the method for various cell culture platform, as well as saving time and resources. In particular, the effects of structural change on the surface and mechanical properties of individual collagen fibrils and matrix networks of collagen were quantitatively assessed at the nano-scale using the AFM. The results present in this chapter can be used to gain a better understanding of the surface and nanomechanical properties of collagen which might be sensed by cells and influence cell behavior. In addition, the approach for characterization of the nanomechanical properties of collagen specimens in this chapter is expected to provide useful information for more accurate nanomechanical properties measurement of biological materials with fibrillar structures such as collagen based on understanding of relationship between their structure and mechanical properties.

5.2 Experimental details

5.2.1 Preparation of collagen specimens

Collagen specimens were prepared from rat tail collagen type I. In brief, the stock collagen solution was added to a mixture of 10X phosphate buffered saline (PBS) and 1N sodium hydroxide. Also, 20 μ M 4-(2-hydroxyethyl)-1-piperazineethanesulfonic acid (HEPES) was added to the mixture to maintain the physiological ionic strength and pH at 7.2-7.6. The volume of collagen solution was controlled by adding deionized water (DIW). The structure of collagen fibrils was modified by replacing a fraction of DIW with an acid-base neutralization solution (N-solution) to archive the target concentration. The N-solution was prepared based on neutralization reaction of 1N sulfuric acid and 1N sodium hydroxide, which results in sodium sulfate and water. The final pH of N-solution was 7.4. Collagen specimens with modified structure were prepared by adding amounts of N-solution equal to 20% and 50% of the final volume. For collagen matrix specimen preparation, the final concentration of collagen solutions was controlled at 1 mg/mL. Also, 0.1 mg/mL collagen solutions were prepared for individual fibril measurements. Collagen solutions were prepared and kept on ice to prevent un-controlled polymerization. Finally, the collagen solution was polymerized for 30 min at 37 °C in a CO₂ incubator.

Collagen specimens for AFM measurements of individual fibrils were prepared as previously described [120]. Briefly, 20 μ L of the polymerized collagen solution with the concentration of 0.1 mg/mL was placed on a microscope slide. After 20 minutes, the specimen was gently rinsed using DIW to remove unattached material and salt residues. The specimens for force-indentation curve measurements were then covered with 1X PBS, before use in AFM measurements. Also, for AFM topographical imaging in air, specimens

were dried for 24 h at room temperature. To prepare collagen matrices AFM force-indentation curve measurements, 60 μL of 1 mg/mL collagen solution was pipetted onto a PDMS washer with inner diameter of about 5 mm attached on the bottom of a petri dish prior to polymerization using the incubator. The polymerized specimens were then covered with 1X PBS before use in AFM measurements. In addition, dehydrated collagen matrices were also prepared for AFM topographical imaging in air. 60 μL of 1 mg/mL polymerized collagen was deposited onto a microscope slide. After that, the specimens were fixed with 4% paraformaldehyde for about 1 h. The specimens were then rinsed two times using 1X PBS and three times using DIW and followed by an ethanol/DIW series dehydration with increasing volume percentage of ethanol (30%, 50%, 70%, and 100%) for 15 min per each stage. In the next step, the specimens were incubated in 50% and then 100% hexamethyldisilazane in ethanol for 15 min per each stage. Finally, the specimens were air-dried for 24 h at room temperature.

5.2.2 AFM topographical imaging

AFM measurements were performed using an AFM. Topographical imaging of collagen matrices and individual collagen fibrils were performed in ambient conditions from intermittent contact mode of AFM using Si probes with nominal spring constant of 2 N/m (AC240, Olympus). From the AFM amplitude images obtained on individual fibrils, D-bandings of collagen fibrils were determined given that amplitude signal is more sensitive to difference in height topography [121,122], which is expected to be helpful in obtaining the banding patterns of the collagen fibrils. In addition, from the AFM height images obtained on the collagen matrices, the width of collagen fibril was determined

through the cross-sectional height profile taken perpendicular to the fibril long axis. Also, Abbott-Firestone curve, or material ratio curve, was determined from the AFM image to characterize the difference in surface structures of collagen matrix specimens.

5.2.3 AFM force-indentation curve measurements

For the force-indentation curve measurements on individual collagen fibrils in PBS, 0.1 mg/mL polymerized collagen deposited on microscope slide was used. The specimens were allowed to equilibrate for 2 h in PBS using a closed fluid cell before data was collected to minimize the uncertainties associated with thermal drift of AFM [75]. Individual collagen fibrils were identified from intermittent contact mode imaging in PBS using a 20-nm-thick gold-coated silicon nitride probe with a nominal spring constant of 0.03 N/m (Biolever, Olympus). The shape of the tip was characterized using SEM imaging. The tip had a parabolic shape with a radius of curvature of 20 nm at the apex. The used of a tip with about 20 nm radius was expected to reduce the contact pressure while maintaining the spatial resolution of the tip for topography measurements. After taking a topography image of individual collagen fibril, the force mapping mode of AFM were used to collect the force-indentation curves using the same probe. A total number of 32×32 force-distance curves were collected on an area of $500 \text{ nm} \times 500 \text{ nm}$ over an individual fibril lying on the microscope slide. The maximum normal force was set to 0.5 nN and displacement speed was kept constant at 500 nm/s. Prior to data collection, the deflection sensitivity of the probe was determined from the force-distance curve obtained on a rigid substrate. Also, the spring constant of the probe was obtained based on the thermal noise method [45]. Details information of normal force calibration procedure for measurements in PBS is similar to

that of in electrolyte, as aforementioned (section 4.2.2). The force-displacement data were converted into force-indentation data by subtracting cantilever deflection from displacement. About 40 force-indentation curves obtained on individual collagen fibrils were selected manually based on the force mapping height images for determination of the mechanical properties based on contact model. To avoid artifacts due to geometric effects between curved fibril and the AFM tip [3,123], only the force-indentation curves collected from the center of the fibril were selected for data analysis. After the force-indentation curve measurements, AFM images of the force mapping locations were examined to determine whether plastic deformation occurred.

Force-indentation curve measurements on collagen matrices were performed using a colloidal probe to obtain information about mechanical properties over a larger area. A polystyrene (PS) spherical particle was glued onto an AFM probe with a nominal spring constant of 0.2 N/m (PPP-CONT, Nanosensors). The radius of the PS spherical particle determined from SEM image was 50 μm . About 30 force-indentation curves were obtained on randomly selected locations on the matrices. The experiments were performed under a normal force range from 0.5 nN to 0.8 nN and a constant speed of 1 $\mu\text{m/s}$. The deflection sensitivity and the spring constant of the colloidal probe were determined as aforementioned.

5.3 Surface structures

Figure 5.1 shows AFM images of individual collagen fibrils with 0%, 20%, and 50% N-solution. The height and amplitude images are shown in Figs. 5.1 (a) and 5.1 (b), respectively. The cross-sectional amplitude profiles taken along the fibrils are also included

in Fig. 5.1 (b). The D-banding of collagen fibril was observed for all specimens, as shown in Figs. 5.1 (a) and (b). However, it can be clearly seen from Figs. 5.1 (a) and 5.1 (b) that the banding patterns were more clearly observed from the amplitude images than the height images due to the more sensitivity to difference in height topography of amplitude images [121,122]. In this regard, the amplitude images were used to determine the D-bandings of individual collagen fibrils. To reduce the uncertainty associated with difficulty of small distance determination of a single D-banding, cross-sectional amplitude profile along a few D periods were taken and the D-banding was calculated by dividing the total measured length over the number of D periods. Five different individual fibrils were selected to

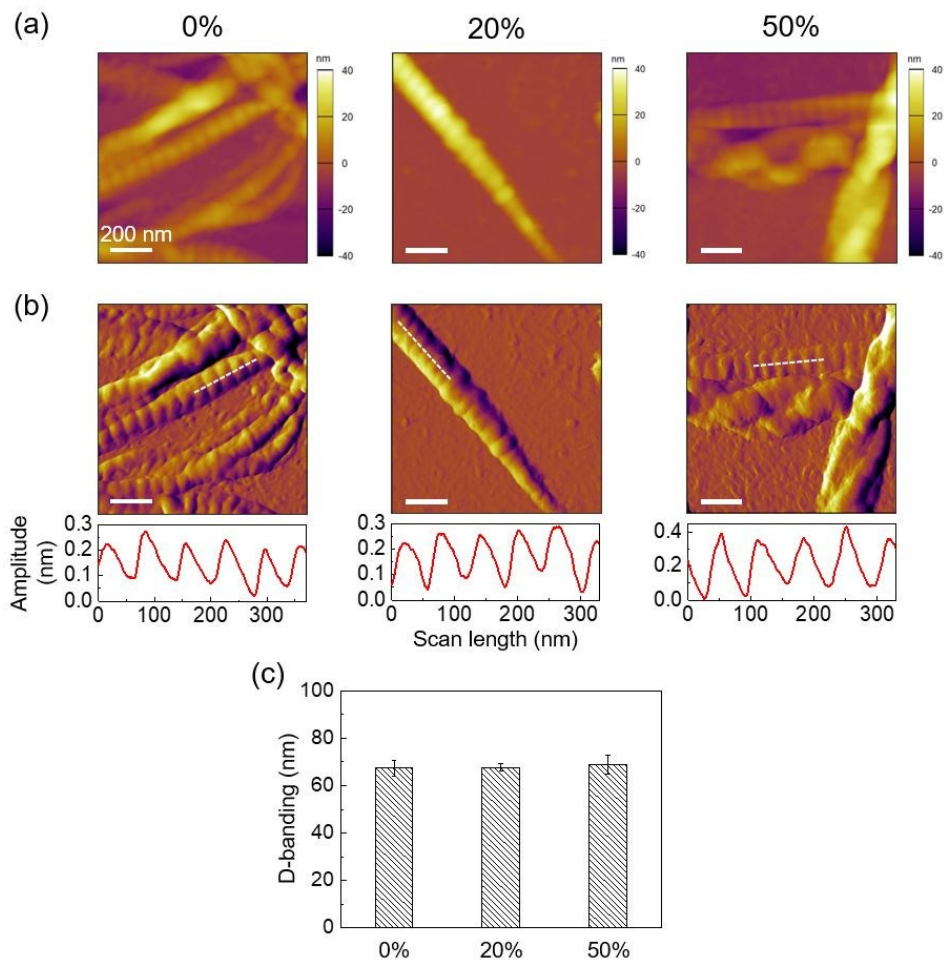


Fig. 5.1. (a) AFM height images, (b) AFM amplitude images, and (c) D-bandings of the collagen fibrils with 0%, 20%, and 50% N-solution.

determine average D-banding for each specimen. Given that the change in direction of fibrils (e.g., twist and bend) may readily affect D-banding observation [124,125], only relatively straight individual fibrils were selected for calculation. The D-banding measurement result of collagen fibrils with 0%, 20%, and 50% N-solution is summarized in Fig. 5.1 (c). The D-banding of collagen fibrils with 0%, 20%, and 50% N-solution was calculated to be 67 ± 3 nm, 68 ± 2 nm, and 69 ± 4 nm, respectively, as shown in Fig. 5.1 (c).

Figure 5.2 (a) shows AFM height images of collagen matrices with 0%, 20%, and 50% N-solution along with the cross-sectional height profiles for each specimen. The height images show that the surface structures of the specimens were different. In general, a relatively uniform matrix network constituted by individual collagen fibrils was observed for specimen without N-solution, similar to those typically observed in literature [110]. In contrast, for specimens with 20% and 50% N-solution, bundles of collagen fibrils were observed, along with an increase of fibril width, as can be seen from the height images and cross-sectional height profiles in Fig. 5.2 (a). Fig. 5.2 (c) shows the averages of width of collagen fibril determined from about 100 collagen fibrils obtained at ten randomly selected locations. The widths of collagen fibrils were calculated to be 104 ± 25 nm, 151 ± 36 nm, and 162 ± 49 nm for collagen matrices with 0%, 20%, and 50% N-solution, respectively. The fibril width was found to increase with increasing concentration of N-solution. The material ratio curves of collagen matrices with 0%, 20%, and 50% N-solution determined from the AFM height images in Fig. 5.2 (a) are presented in Fig. 5.2 (c). For a clear comparison between the specimens, the zero-material point was defined at the highest peak on the surface of each specimen, the material ratio or percentage of material traversed in relation to the area covered is then calculated by moving a horizontal plane from the highest

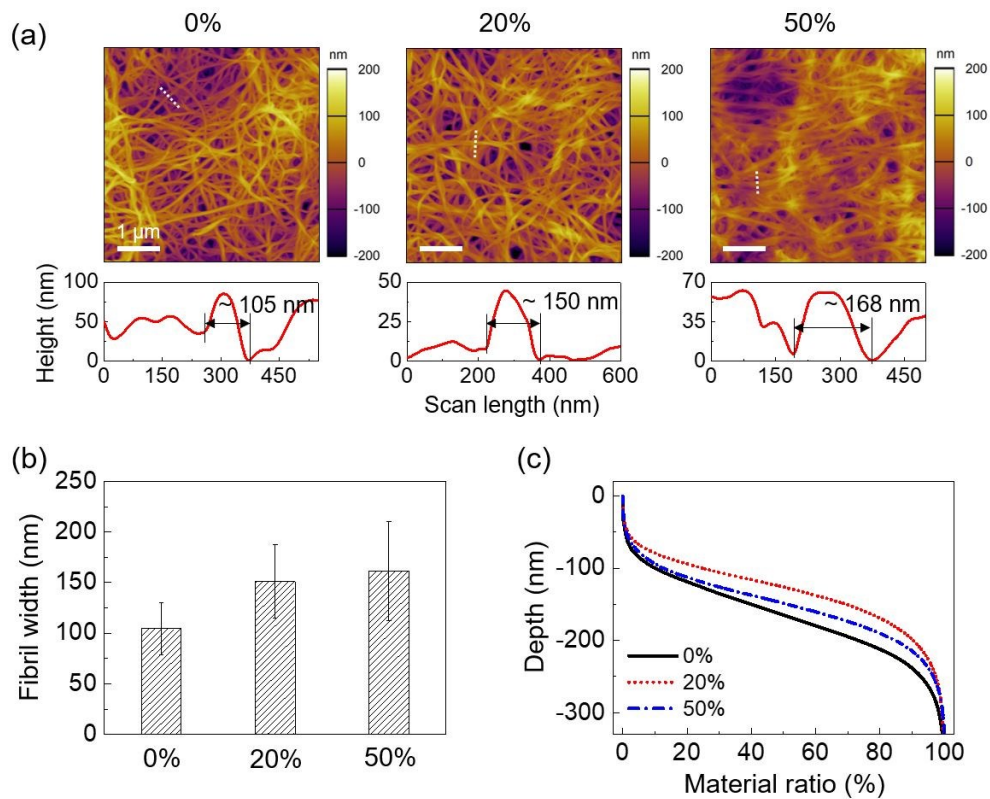


Fig. 5.2. (a) AFM height images, (b) fibril widths, and (c) material ratio curves of the collagen matrices with 0%, 20%, and 50% N-solution. The material curve represents the percentage of material traversed in relation to the area covered.

peak (0% material) to the lowest valley (100% material) on the surface. It was found that the shapes of material ratio curves are different for all specimens, likely due to difference in surface structures of the specimens. In general, the material ratio curve was steeper for specimen with 0% N-solution than those of 20% and 50% N-solution. Also, the material curve for 50% was slightly steeper than that of 20% N-solution.

5.4 Nanomechanical properties

5.4.1 Elastic modulus of individual collagen fibrils

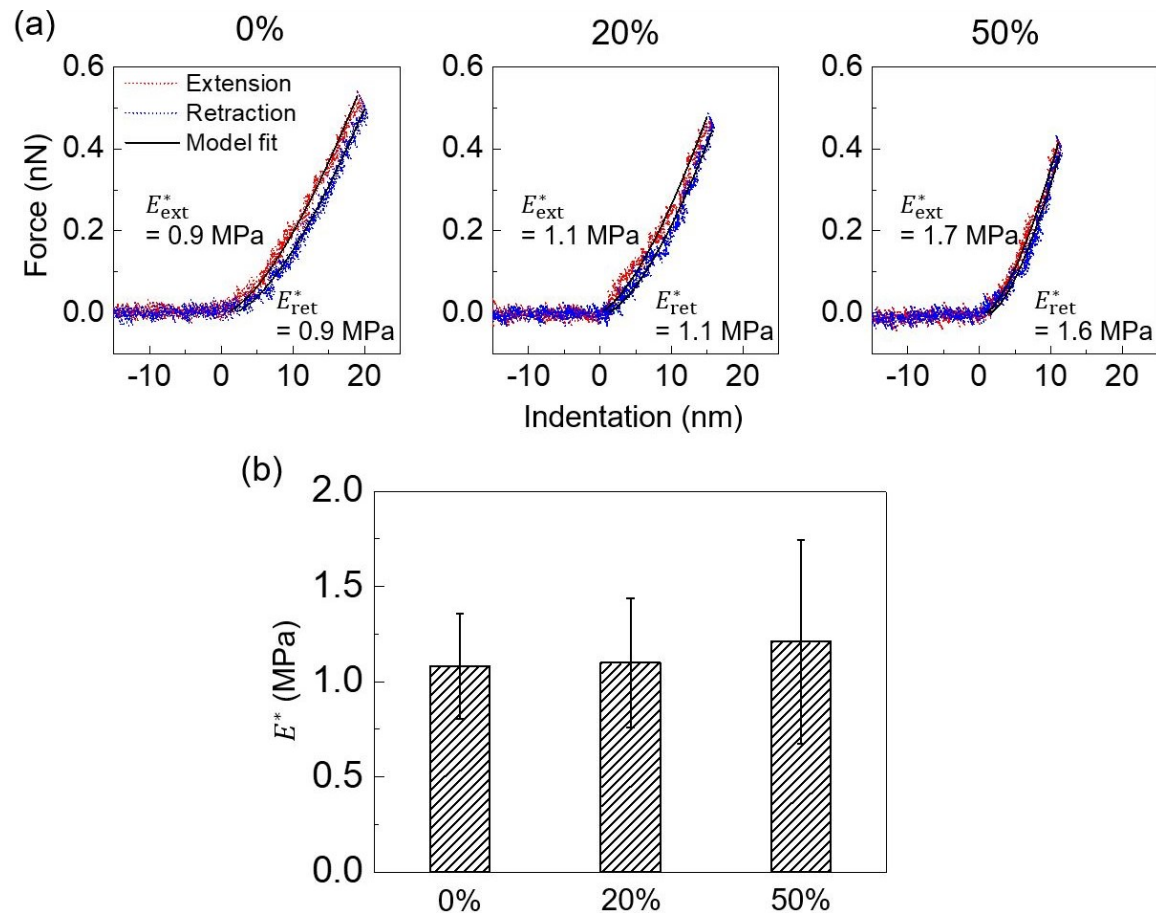


Fig. 5.3. (a) Force-indentation curves and (b) mean elastic modulus of the collagen fibrils with 0%, 20%, and 50% N-solution.

Figure 5.3 (a) shows force-indentation curves obtained on individual collagen fibrils with 0%, 20%, and 50% N-solution. The pull-off force was not clearly observed for all specimens, as shown in Fig. 5.3 (a). Also, as shown in Fig. 5.3 (a), the indentation depths of the specimens ranged from 12 nm to 19 nm and were comparable to the curvature radius at the apex of the tip. In this regard, Sneddon's model [126] for a parabolic shaped tip was used to obtain E^* of the collagen fibrils. The relationship between F and δ can be obtained from Eq. (5.1), based on the Sneddon's model.

$$F = \frac{4}{3} R^{1/2} E^* \delta^{3/2}. \quad (5.1)$$

Also, since the elastic modulus of the tip was significantly larger than that of the collagen specimens used, E^* can be approximated by $E^* \approx E_s/(1 - \nu_s^2)$.

As can be observed in Fig. 5.3 (a), force-indentation curves obtained on collagen fibrils exhibit no significant hysteresis, which suggests that the effect of friction on force-indentation data is negligible. In addition, no significant residual deformation was observed on the collagen fibrils after force-indentation curve measurements, as shown in Fig. 5.4. Hence, elastic contact between the tips and the collagen fibrils during force-indentation curve measurements was assumed. E^* of collagen fibrils with 0%, 20%, and 50% N-solution was obtained from both extension and retraction curves. The fit results based on Sneddon's model are shown in Fig. 5.3 (a). It can be seen that the Sneddon's model fits agreed with the force-indentation data for all specimens, which suggests that elastic contact occurred during force-indentation curve measurement [5]. The averages of E^* were calculated to be 1.1 ± 0.3 MPa, 1.1 ± 0.3 MPa, and 1.2 ± 0.5 MPa for the collagen fibrils with 0%, 20%, and 50% N-solution, respectively, as shown in Fig. 5.3 (b).

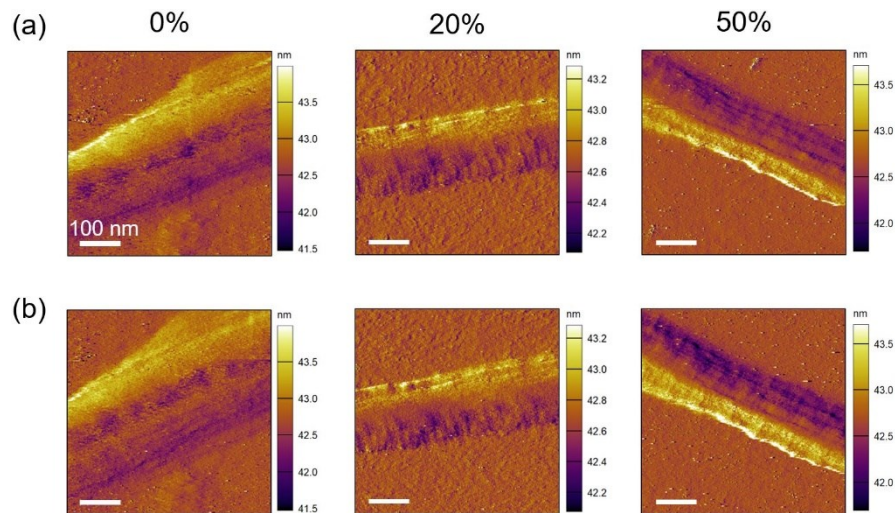


Fig. 5.4. AFM amplitude images of the collagen fibrils with 0%, 20%, and 50% N-solution (a) before and (b) after force-indentation curve measurements.

5.4.2 Elastic modulus of collagen matrices

Figure 5.5 (a) shows force-indentation curves obtained on collagen matrices with 0%, 20%, and 50% N-solution. A hysteresis between extension and retraction data was clearly observed for all specimens, indicating of large adhesion presence between the colloidal probe and collagen matrices, as observed in previous work [3]. However, the reproducibility of force-indentation curves obtained at same locations suggests a largely elastic response of the matrix networks, as shown in Fig. 5.6. The indentation depths of the specimens ranged from about 7 μm to 9 μm , correspond to the normal force from about 0.5

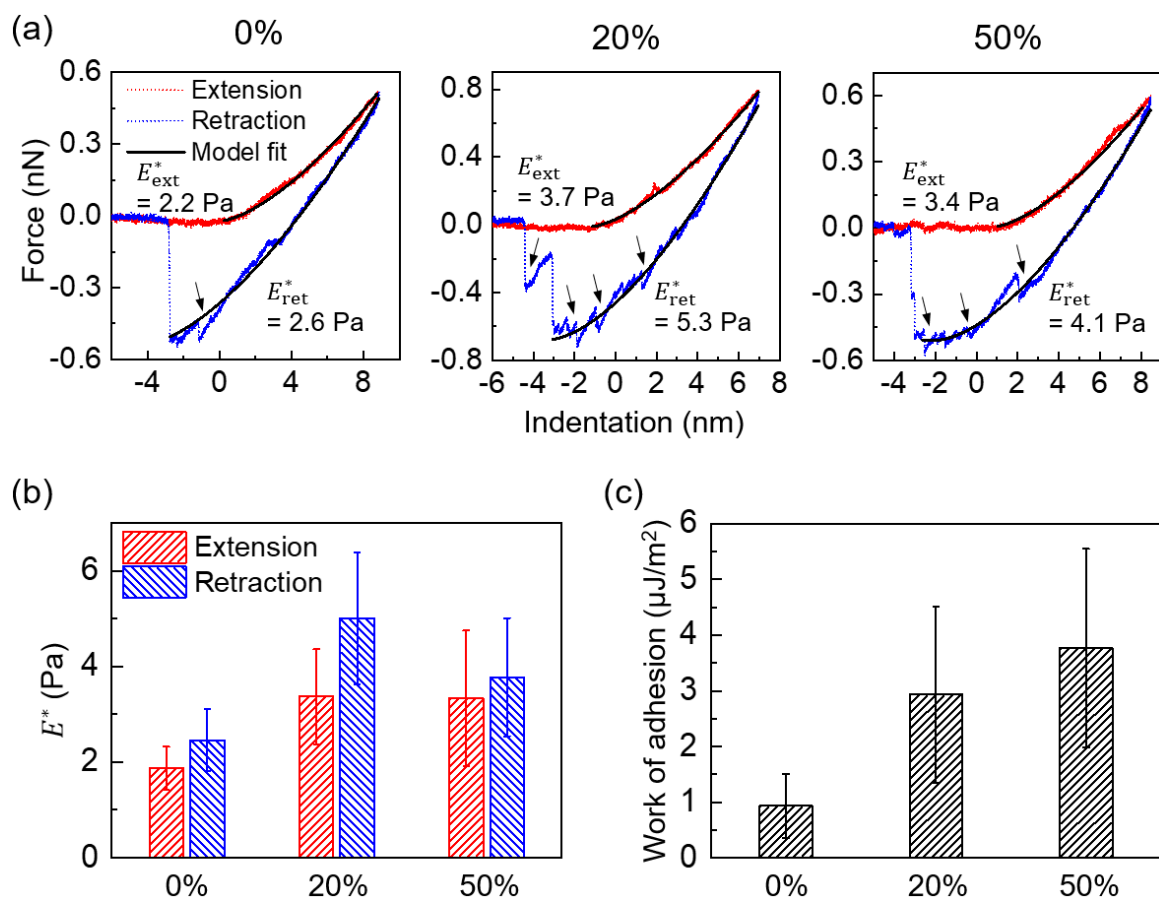


Fig. 5.5. (a) Force-indentation curves, (b) mean elastic modulus, and (c) works of adhesion of the collagen matrices with 0%, 20%, and 50% N-solution. In (a), the black arrows indicate that the number of adhesion events is higher for matrices with 20% and 50% N-solution than that of 0% N-solution.

nN to 0.8 nN, as shown in Fig. 5.5 (a). To consider the adhesion, force-indentation curves obtained on collagen matrices with 0%, 20%, and 50% N-solution were fit using the JKR model [52]. E_{ext}^* and E_{ret}^* were calculated to be 2.2 Pa and 2.6 Pa, 3.7 Pa and 5.3 Pa, and 3.4 Pa and 4.1 Pa for the collagen matrices with 0%, 20%, and 50% N-solution, using the data shown in Fig. 5.5 (a). E^* values determined from extension curves were generally smaller than those of retraction curves as a result of hysteresis in force-indentation data, as shown in Fig. 5.5 (a). E_{ext}^* and E_{ret}^* determined from 30 force-indentation curves are summarized in Fig. 5.5 (b). The averages of E_{ext}^* were 1.9 ± 0.5 Pa, 3.4 ± 1 Pa, and 3.3 ± 1.4 Pa for 0%, 20%, and 50% N-solution specimens, respectively. Also, averages of E_{ret}^* for 0%, 20%, and 50% N-solution specimens were calculated to be 2.5 ± 0.7 Pa, 5 ± 1.4 Pa, and 3.8 ± 1.2 Pa, respectively. Fig. 5.5 (c) shows the work of adhesion determined from

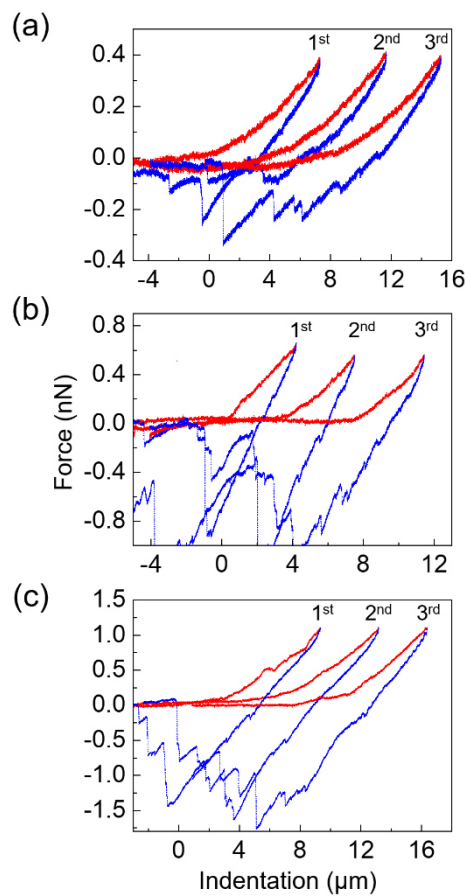


Fig. 5.6. Examples of force-indentation curves measured continuously at same locations on the collagen matrices with (a) 0%, (b) 20%, and (c) 50% N-solution.

curve fits to the retraction curves for collagen matrices with 0%, 20%, and 50% N-solution. The average values of work of adhesion determined from retraction curve fits were $0.9 \pm 0.6 \mu\text{J}/\text{m}^2$, $2.9 \pm 1.6 \mu\text{J}/\text{m}^2$, and $3.8 \pm 1.8 \mu\text{J}/\text{m}^2$ for collagen matrices with 0%, 20%, and 50% N-solution, respectively. It was found that the work of adhesion of the specimens increased with increasing N-solution concentration. Also, a significantly higher number of adhesion events were observed in force-indentation curves obtained on matrices with 20% and 50% N-solution, compared to that of 0% N-solution, as can be clearly seen in Fig. 5.5 (a). It is plausible that for the specimen with 0% N-solution, the collagen fibrils are firmly linked to each other to form a relatively uniform matrix of fibril, as shown in Fig. 5.2 (a), while the link may be loosened for matrices of bundled fibrils. As a result, more fibrils may attach to the AFM tip, leading to increase in adhesion with increasing N-solution concentration, as shown in Figs. 5.5 (a) and (c). It is plausible that the collagen fibrils can be detached gradually when the tip retract from the surface, causing an increase in number of adhesion events in the force-indentation data obtained on matrices with 20% and 50% N-solution.

5.4.3 Effects of structural modification

Table 5.1 shows the summary of reduced elastic moduli determined for the individual collagen fibrils and collagen matrices with 0%, 20%, and 50% N-solution. The reduced elastic moduli of collagen fibrils and collagen matrices in this work are in similar order of magnitude compared to those typically obtained for collagen fibrils [120,123] and collagen matrices [127,128], respectively, in literature. As can be seen in Table 5.1, no significant different was observed between the E_{ext}^* and E_{ret}^* values of individual collagen fibrils with

Table 5.1 Summary of the reduced elastic moduli determined for the individual collagen fibrils and collagen matrices with 0%, 20%, and 50% N-solution.

Specimen	Individual collagen fibril			Collagen matrix		
	E_{ext}^* (MPa)	E_{ret}^* (MPa)	E^* (MPa)	E_{ext}^* (Pa)	E_{ret}^* (Pa)	E^* (Pa)
0%	1.0 ± 0.6	1.1 ± 0.3	1.1 ± 0.3	1.9 ± 0.5	2.5 ± 0.7	2.1 ± 0.5
20%	1.1 ± 0.2	1.1 ± 0.3	1.1 ± 0.3	3.4 ± 1.0	5.0 ± 1.4	4.2 ± 1.0
50%	1.2 ± 0.5	1.2 ± 0.6	1.2 ± 0.5	3.3 ± 1.4	3.8 ± 1.2	3.6 ± 1.2

0%, 20%, and 50% N-solution. Also, the reduced elastic moduli of collagen fibrils with 0%, 20%, and 50% N-solution agreed with each other. In contrast, the reduced elastic moduli of collagen matrices with 0%, 20%, and 50% N-solution showed different patterns. In particular, reduced elastic moduli was found to increase with increasing N-solution concentration up to 20% N-solution, while a slight reduction of reduced elastic modulus was observed at 50% N-solution. The reduced elastic moduli of 0% N-solution matrix was smaller by factors of 2 and 1.7 than 20% and 50% N-solution matrices, respectively. Also, the reduced elastic moduli determined from the extension curves were smaller compared to those from the retraction curves, due to the effect of relatively large adhesion between the tip and collagen matrices in retraction.

In contrast to the mechanical properties of individual collagen fibrils, the mechanical properties of collagen matrices were found to be altered due to N-solution. It is clear from the AFM images obtained on collagen matrices that the width of bundles of collagen fibrils increase with increasing N-solution concentration, as can be observed in Fig. 5.2. The increase in the width of collagen fibrils was expected to result in increase in mechanical properties of collagen matrices in the same order. However, the tendency of mechanical

properties of collagen matrices in relation to the increasing concentration of N-solution was differ from what expected (reduced elastic modulus: $0\% < 50\% < 20\%$). Interestingly, the tendency of matrices mechanical properties was found to correlate with that of material ratio (e.g., material ratio: $0\% < 50\% < 20\%$ at 150 nm depth). Given that the material ratio represents the amount of material at a given depth, higher material ratio of collagen matrix with 20% N-solution may be responsible for higher mechanical properties, compared with those of matrices with 0% and 50% N-solution. In other word, higher material ratio may be corresponding to higher density of the collagen matrix and, therefore, result in enhanced mechanical properties. The results also suggest that the effect of increase of fibril width on mechanical properties of fibrillar matrix is not significant in this work.

5.5 Discussion and summary

In this chapter, a new method for modification of structure of collagen network is proposed. By incorporating the sulfate anion during the polymerization process of collagen, the structure of collagen fibrils is controlled into bundles. The width of fibril bundle was found to increase with increasing concentration of sulfate anion. It is postulated that the sulfate ions can bind to individual collagen fibrils through specific sites inside the fibrils [119], which may in turn cause electrostatic attraction between individual fibrils, leading to formation of bundles.

The effect of structural modification of collagen fibrils on nanomechanical properties of individual collagen fibrils and collagen matrix networks were quantitatively assessed using AFM to gain a fundamental understanding of the cell response to change in mechanical properties of collagen. The result showed that similar D-bandings were

observed for collagen fibrils with 20% and 50% N-solution, compared to that of 0% N-solution, suggesting that the addition of N-solution had no significant effect on the collagen fibril formation process. Also, the calculation results for D-banding of specimens were consistent with the value typically observed in literature for collagen type I [120,122].

The result from topographical imaging (Fig. 5.1) and force-indentation curve measurements (Fig. 5.3) on fibrils with 0%, 20%, and 50% N-solution suggest that the addition of N-solution had no significant effect on the morphology and intrinsic mechanical properties of individual collagen fibrils. However, the force-indentation curve measurement results on matrices of collagen fibrils showed increase in mechanical properties of collagen matrices due to addition of N-solution. In particular, the mechanical properties of collagen matrix specimens in this work were found to correlate with the material ratio curve of each specimen. The outcome is useful for understanding of mechanical behavior of specimen with fibril network structure (e.g., matrices of collagen type I).

In general, the structure and mechanical properties of collagen matrix networks were found to be altered due to addition of N-solution. We have examined the effect of change of structure and mechanical properties of collagen matrices on the cell response in a separate study [130]. The morphology and behavior of human cervical cancer (HeLa) cells cultured on collagen matrices with 0%, 20%, and 50% N-solution were quantitatively investigated. The cell area and perimeter were found to generally decrease in the presence of N-solution. Also, the decrease in migration speed along with a more random walk motion were observed for HeLa cells cultured on collagen matrices with 20% and 50% N-solution, suggesting that bundled structure of collagen may inhibit the cell migration. The outcome is expected to be helpful in prediction of cancer cell invasion and metastasis.

It should be noted that the effect of N-solution-based structural modification on mechanical properties of the modified collagen network should be more systematically investigated to attain further understanding in the relationship between structural and mechanical properties of collagen fibrils and cell behavior. In addition, the effects of structural modification on lateral stiffness of collagen fibrils and collagen matrices need to be explored, given that lateral stiffness is also an important factor that regulates the cell behaviors [3,112]. Furthermore, more works is needed to clarify the mechanisms of collagen bundles formation and the relationship between structural change of collagen and cell behaviors. Nevertheless, the method for control of the collagen structure proposed in this work may be useful for future study on metastatic process of cancer. In addition, the approach used in this chapter may be useful for more accurate measurement of nanomechanical properties of biological materials, especially for materials with fibrillar structures.

Chapter 6 Conclusions and recommendations

6.1 Conclusions of the research

In summary, this research focuses on measurements of nanomechanical properties of soft materials using AFM force-indentation curves. Based on better understanding of the interaction between the AFM probe and specimen, the approach was expected to provide useful information for accurate nanomechanical properties measurements using AFM. In particular, the research provides information for AFM tip selection and characterization, and data interpretation to determine the mechanical properties of target specimen. In addition, the AFM-based indentation technique is applied to understand the nanomechanical properties of thin film and fibrillar structures, which are typical structures of soft and biological materials, respectively. Based on the results presented in this research, the following conclusions are drawn:

1. The effect of tip shape on nanomechanical properties measurements was systematically investigated using four different AFM tip with spherical and flat-ended tips, and conical tips with rounded apexes. It was found that the probe with a flat ended tip was prone to misalignment even with the specimen with a few nm of surface roughness, suggesting that the flat ended tip may not appropriate for nanomechanical properties measurements. In addition, a significant different between the extension and retraction curves was observed in the force-indentation curves obtained using the spherical tip and conical tips with rounded apexes, feasibly due to the friction between the tip and specimen. To minimize the effect of friction, as well as reduce uncertainties associated with tip characterization, and force and indentation measurements, the probe with relatively large tip radius (e.g., ~ 30 nm) and minimal spring constant was recommended for mechanical properties measurement of specimen with a few GPa elastic modulus.

2. AFM-based indentation method was applied to measure the nanomechanical properties of soft materials such as polymer binders for LIBs. Considering the practical application of polymer binder in LIBs, the mechanical properties of polymer binder were quantitatively measured in both air and electrolyte. In contrast to the force-indentation curves obtained in air, the effect of friction on force-indentation curves obtained in electrolyte was negligible and can be associated with the significant decrease in friction characteristics of the specimens due to immersion in electrolyte. The outcomes may be helpful to develop polymer binders for improved electrochemical stability of electrodes for LIBs based on understanding of the effect of electrolyte on material properties of polymer binders. The procedure for force-indentation curve measurements and data interpretation in electrolyte can also be used for accurate measurement of mechanical properties of soft materials (e.g., polymer thin films) at the nano-scale.

3. The application of force-indentation curve measurement to determine the mechanical properties of biological materials, which often have the fibrillar structures such as collagen is also presented. The nanomechanical properties of collagen were experimentally investigated to gain a fundamental understanding of the effect of structural change of collagen fibrils on their mechanical properties that can regulate the cell behaviors. The mechanical properties of the fibrillar network of collagen were found to correlate with the material ratio curve, which may be used to understand the response of the fibrillar network to the force applied by the AFM tip. The outcome can be used to gain better understanding of mechanical behavior of materials that have fibril network structures. In addition, the method for control of the collagen structure into bundles can be used for various cell culture platform, especially the platform used for studying the metastasis process of cancer.

6.2 Recommendations for future work

Overall, the approaches used in this research would be useful for accurate measurements of nanomechanical properties of soft and biological materials using the AFM. Despite the contributions of these findings, some interesting and important directions for future studies remain, which are described as follows:

1. To determine the mechanical properties of specimens, adhesive contact models without consideration of friction was used due to the lack of adhesive contact model that consider friction. Given that the energy dissipation due to friction may readily occur and can cause systematic uncertainty in the elastic modulus, theoretical approaches to compensate for the effect of friction on force-indentation data are needed.

2. As for the polymer binders for LIBs, the frictional behaviors between the polymer binder and electrode components need to be clearly understood, given that the contact shearing and sliding between polymer binder and electrode components may be occur during the lithiation and delithiation processes.

3. The role of anion binding in collagen bundle formation should be clearly understood to add further insights into the structure and mechanical properties of collagen fibrils that regulate the cell behaviors. In addition, the studies on effects of structural modification using N-solution on the viscoelastic and frictional properties of the collagen fibrils are also interesting topics, which may be needed to further clarify the relationship between properties of collagen and the cell behaviors.

REFERENCES

- [1] A. Magasinski, B. Zdyrko, I. Kovalenko, B. Hertzberg, R. Burtovyy, C.F. Huebner, T.F. Fuller, I. Luzinov, G. Yushin, Toward Efficient Binders for Li-Ion Battery Si-Based Anodes: Polyacrylic Acid, *ACS Appl. Mater. Interfaces* 2 (2010) 3004-3010.
- [2] I. Kovalenko, B. Zdyrko, A. Magasinski, B. Hertzberg, Z. Milicev, R. Burtovyy, I. Luzinov, G. Yushin, A Major Constituent of Brown Algae for Use in High-Capacity Li-Ion Batteries, *Science* 334 (2011) 75-79.
- [3] K.-H. Chung, K. Bhadriraju, T.A. Spurlin, R.F. Cook, A.L. Plant, Nanomechanical Properties of Thin Films of Type I Collagen Fibrils, *Langmuir* 26 (2010) 3629-3636.
- [4] B. Cappella, *Mechanical Properties of Polymers Measured through AFM Force-Distance Curves*, Springer International Publishing, 2016.
- [5] H.-J. Butt, B. Cappella, M. Kappl, Force measurements with the atomic force microscope: Technique, interpretation and applications, *Surf. Sci. Rep.* 59 (2005) 1-152.
- [6] C.A. Clifford, M.P. Seah, Quantification issues in the identification of nanoscale regions of homopolymers using modulus measurement via AFM nanoindentation, *Appl. Surf. Sci.* 252 (2005) 1915-1933.
- [7] D. Passeri, A. Alippi, A. Bettucci, M. Rossi, E. Tamburri, M.L. Terranova, Indentation modulus and hardness of polyaniline thin films by atomic force microscopy, *Synth. Met.* 161 (2011) 7-12.
- [8] U. Rabe, W. Arnold, Acoustic microscopy by atomic force microscopy, *Appl. Phys. Lett.* 64 (1994) 1493-1495.
- [9] K. Yamanaka, S. Nakano, Ultrasonic atomic force microscope with overtone excitation of cantilever, *Jpn. J. Appl. Phys.* 35 (1996) 3787.
- [10] O. Sahin, S. Magonov, C. Su, C.F. Quate, O. Solgaard, An atomic force microscope tip designed to measure time-varying nanomechanical forces, *Nat. Nanotechnol.* 2 (2007) 507.
- [11] D. Passeri, A. Bettucci, M. Germano, M. Rossi, A. Alippi, S. Orlanducci, M.L. Terranova, M. Ciavarella, Effect of tip geometry on local indentation modulus measurement via atomic force acoustic microscopy technique, *Rev. Sci. Instrum.* 76 (2005) 093904.
- [12] M. Chyasnavichyus, S.L. Young, R. Geryak, V.V. Tsukruk, Probing elastic properties of soft materials with AFM: Data analysis for different tip geometries, *Polymer* 102 (2016) 317-325.
- [13] L.-Y. Lin, D.-E. Kim, Measurement of the elastic modulus of polymeric films using an AFM with a steel micro-spherical probe tip, *Polym. Test.* 31 (2012) 926-930.
- [14] M. Kopycinska-Müller, R.H. Geiss, D.C. Hurley, Contact mechanics and tip shape in AFM-based nanomechanical measurements, *Ultramicroscopy* 106 (2006) 466-474.

- [15] J.P. Killgore, R.H. Geiss, D.C. Hurley, Continuous Measurement of Atomic Force Microscope Tip Wear by Contact Resonance Force Microscopy, *Small* 7 (2011) 1018-1022.
- [16] J.H. Hoh, A. Engel, Friction effects on force measurements with an atomic force microscope, *Langmuir* 9 (1993) 3310-3312.
- [17] P. Attard, A. Carambassis, M.W. Rutland, Dynamic Surface Force Measurement. 2. Friction and the Atomic Force Microscope, *Langmuir* 15 (1999) 553-563.
- [18] J. Stiernstedt, M.W. Rutland, P. Attard, A novel technique for the in situ calibration and measurement of friction with the atomic force microscope, *Rev. Sci. Instrum.* 76 (2005) 083710.
- [19] K.-H. Chung, G.A. Shaw, J.R. Pratt, Accurate noncontact calibration of colloidal probe sensitivities in atomic force microscopy, *Rev. Sci. Instrum.* 80 (2009) 065107.
- [20] J.R. Pratt, G.A. Shaw, L. Kumanchik, N.A. Burnham, Quantitative assessment of sample stiffness and sliding friction from force curves in atomic force microscopy, *J. Appl. Phys.* 107 (2010) 044305.
- [21] A. Yacoot, L. Koenders, Recent developments in dimensional nanometrology using AFMs, *Meas. Sci. Technol.* 22 (2011) 122001.
- [22] M.E. Dokukin, I. Sokolov, On the Measurements of Rigidity Modulus of Soft Materials in Nanoindentation Experiments at Small Depth, *Macromolecules* 45 (2012) 4277-4288.
- [23] S. Tan, R.L. Sherman, W.T. Ford, Nanoscale Compression of Polymer Microspheres by Atomic Force Microscopy, *Langmuir* 20 (2004) 7015-7020.
- [24] H.K. Nguyen, S. Fujinami, K. Nakajima, Elastic modulus of ultrathin polymer films characterized by atomic force microscopy: The role of probe radius, *Polymer* 87 (2016) 114-122.
- [25] A. Solmaz, T. Aytun, J.K. Deuschle, C. Ow-Yang, Nanoscale Elastic Modulus Variation in Loaded Polymeric Micelle Reactors, *Langmuir* 28 (2012) 10592-10596.
- [26] B.B. Akhremitchev, G.C. Walker, Finite Sample Thickness Effects on Elasticity Determination Using Atomic Force Microscopy, *Langmuir* 15 (1999) 5630-5634.
- [27] Y. Sun, B. Akhremitchev, G.C. Walker, Using the Adhesive Interaction between Atomic Force Microscopy Tips and Polymer Surfaces to Measure the Elastic Modulus of Compliant Samples, *Langmuir* 20 (2004) 5837-5845.
- [28] J. Domke, M. Radmacher, Measuring the Elastic Properties of Thin Polymer Films with the Atomic Force Microscope, *Langmuir* 14 (1998) 3320-3325.
- [29] A. Touhami, B. Nysten, Y.F. Dufre ne, Nanoscale Mapping of the Elasticity of Microbial Cells by Atomic Force Microscopy, *Langmuir* 19 (2003) 4539-4543.
- [30] W.A. Ducker, T.J. Senden, R.M. Pashley, Direct measurement of colloidal forces using an atomic force microscope, *Nature* 353 (1991) 239-241.

- [31] K.-H. Chung, J.R. Pratt, M.G. Reitsma, Lateral Force Calibration: Accurate Procedures for Colloidal Probe Friction Measurements in Atomic Force Microscopy, *Langmuir* 26 (2010) 1386-1394.
- [32] K.L. Johnson, *Contact Mechanics*, Cambridge University Press, Cambridge, 1985.
- [33] C. Koo-Hyun, L. Yong-Ha, K. Dae-Eun, J. Yoo, S. Hong, Tribological characteristics of probe tip and PZT media for AFM-based recording technology, *IEEE Trans. Magn.* 41 (2005) 849-854.
- [34] K.-H. Chung, Y.-H. Lee, H.-J. Kim, D.-E. Kim, Fundamental Investigation of the Wear Progression of Silicon Atomic Force Microscope Probes, *Tribol. Lett.* 52 (2013) 315-325.
- [35] K.-H. Chung, H.-J. Kim, L.-Y. Lin, D.-E. Kim, Tribological characteristics of ZnO nanowires investigated by atomic force microscope, *Appl. Phys. A* 92 (2008) 267-274.
- [36] K.-H. Chung, Wear characteristics of atomic force microscopy tips: A reievew, *Int. J. Precis. Eng. Manuf.* 15 (2014) 2219-2230.
- [37] G.V. Samsonov, Mechanical Properties of the Elements, in: G.V. Samsonov (Ed.) *Handbook of the Physicochemical Properties of the Elements*, Springer US, Boston, MA, 1968, pp. 387-446.
- [38] M.A. Lantz, S.J. O'Shea, A.C.F. Hoole, M.E. Welland, Lateral stiffness of the tip and tip-sample contact in frictional force microscopy, *Appl. Phys. Lett.* 70 (1997) 970-972.
- [39] J. Merker, D. Lupton, M. Töpfer, H. Knake, High temperature mechanical properties of the platinum group metals, *Platin. Met. Rev.* 45 (2001) 74-82.
- [40] N. Chen, L. Hong, Surface phase morphology and composition of the casting films of PVDF–PVP blend, *Polymer* 43 (2002) 1429-1436.
- [41] K. Backfolk, C. Andersson, J. Peltonen, Association between a sodium salt of a linear dodecylbenzene sulphonate and a non-ionic fatty alcohol ethoxylate surfactant during film formation of styrene/butadiene latex, *Colloids and Surfaces A: Physicochem. Eng. Aspects* 291 (2006) 38-44.
- [42] G. Wypych, PAA poly(acrylic acid), in: G. Wypych (Ed.) *Handbook of Polymers* (Second Edition), ChemTec Publishing, 2016, pp. 251-253.
- [43] S. Castagnet, S. Girault, J.L. Gacougnolle, P. Dang, Cavitation in strained polyvinylidene fluoride: mechanical and X-ray experimental studies, *Polymer* 41 (2000) 7523-7530.
- [44] O. Starkova, A. Aniskevich, Poisson's ratio and the incompressibility relation for various strain measures with the example of a silica-filled SBR rubber in uniaxial tension tests, *Polym. Test.* 29 (2010) 310-318.
- [45] J.L. Hutter, J. Bechhoefer, Calibration of atomic-force microscope tips, *Rev. Sci. Instrum.* 64 (1993) 1868-1873.
- [46] F. Alaa, M. Renate, A. Schönhals, F. Friedrich Jörg, Structure of Plasma-Deposited Poly(acrylic acid) Films, *Plasma Process. Polym.* 8 (2011) 147-159.

- [47] J. Kaszyńska, B. Hilczer, P. Biskupski, Segmental dynamics in poly(vinylidene fluoride) studied by dielectric, mechanical and nuclear magnetic resonance spectroscopies, *Polym. Bull.* 68 (2012) 1121-1134.
- [48] C. Souillard, J.-Y. Cavallé, L. Chazeau, R. Schach, Dynamic mechanical relaxation of cross-linked styrene-butadiene polymers containing free chains: Possibility of reptation, *Polymer* 55 (2014) 5218-5225.
- [49] E. A-Hassan, W.F. Heinz, M.D. Antonik, N.P. D'Costa, S. Nageswaran, C.A. Schoenenberger, J.H. Hoh, Relative microelastic mapping of living cells by atomic force microscopy, *Biophys. J.* 74 (1998) 1564-1578.
- [50] W.C. Oliver, G.M. Pharr, An improved technique for determining hardness and elastic modulus using load and displacement sensing indentation experiments, *J. Mater. Res.* 7 (1992) 1564-1583.
- [51] B.J. Briscoe, L. Fiori, E. Pelillo, Nano-indentation of polymeric surfaces, *J. Phys. D: Appl. Phys.* 31 (1998) 2395.
- [52] K.L. Johnson, K. Kendall, A.D. Roberts, Surface Energy and the Contact of Elastic Solids, *Proc. R. Soc. Lond. A.* 324 (1971) 301-313.
- [53] M. Rundlöf, M. Karlsson, L. Wågberg, E. Poptoshev, M. Rutland, P. Claesson, Application of the JKR Method to the Measurement of Adhesion to Langmuir–Blodgett Cellulose Surfaces, *J. Colloid Interface Sci.* 230 (2000) 441-447.
- [54] J. Notbohm, B. Poon, G. Ravichandran, Analysis of nanoindentation of soft materials with an atomic force microscope, *J. Mater. Res.* 27 (2012) 229-237.
- [55] K. Kendall, The adhesion and surface energy of elastic solids, *J. Phys. D: Appl. Phys.* 4 (1971) 1186.
- [56] C.G.N. Pelletier, E.C.A. Dekkers, L.E. Govaert, J.M.J.d. Toonder, H.E.H. Meijer, The influence of indenter-surface misalignment on the results of instrumented indentation tests, *Polym. Test.* 26 (2007) 949.
- [57] N.B. Shahjahan, Z. Hu, Effects of angular misalignment on material property characterization by nanoindentation with a cylindrical flat-tip indenter, *J. Mater. Res.* 32 (2017) 1456-1465.
- [58] Y.-Y. Lin, C.-F. Chang, W.-T. Lee, Effects of thickness on the largely-deformed JKR (Johnson–Kendall–Roberts) test of soft elastic layers, *Int. J. Solids Struct.* 45 (2008) 2220-2232.
- [59] C.S. Kan, J.H. Blackson, Effect of Ionomeric Behavior on the Viscoelastic Properties and Morphology of Carboxylated Latex Films, *Macromolecules* 29 (1996) 6853-6864.
- [60] K.-H. Chung, Y.-H. Lee, Y.-T. Kim, D.-E. Kim, J. Yoo, S. Hong, Nano-tribological characteristics of PZT thin film investigated by atomic force microscopy, *Surf. Coat. Technol.* 201 (2007) 7983-7991.
- [61] U. Kasavajjula, C. Wang, A.J. Appleby, Nano- and bulk-silicon-based insertion anodes for lithium-ion secondary cells, *J. Power Sources* 163 (2007) 1003.

- [62] L.Y. Beaulieu, T.D. Hatchard, A. Bonakdarpour, M.D. Fleischauer, J.R. Dahn, Reaction of Li with Alloy Thin Films Studied by In Situ AFM, *J. Electrochem. Soc.* 150 (2003) A1457-A1464.
- [63] H. Wu, Y. Cui, Designing nanostructured Si anodes for high energy lithium ion batteries, *Nano Today* 7 (2012) 414-429.
- [64] Y. Park, S. Lee, S.-H. Kim, B.Y. Jang, J.S. Kim, S.M. Oh, J.-Y. Kim, N.-S. Choi, K.T. Lee, B.-S. Kim, A photo-cross-linkable polymeric binder for silicon anodes in lithium ion batteries, *RSC Adv.* 3 (2013) 12625-12630.
- [65] H.S. Yang, S.-H. Kim, A.G. Kannan, S.K. Kim, C. Park, D.-W. Kim, Performance Enhancement of Silicon Alloy-Based Anodes Using Thermally Treated Poly(amide imide) as a Polymer Binder for High Performance Lithium-Ion Batteries, *Langmuir* 32 (2016) 3300-3307.
- [66] M. Ling, J. Qiu, S. Li, C. Yan, M.J. Kiefel, G. Liu, S. Zhang, Multifunctional SA-PProDOT Binder for Lithium Ion Batteries, *Nano Lett.* 15 (2015) 4440-4447.
- [67] A. Sheidaei, X. Xiao, X. Huang, J. Hitt, Mechanical behavior of a battery separator in electrolyte solutions, *J. Power Sources* 196 (2011) 8728-8734.
- [68] G.Y. Gor, J. Cannarella, C.Z. Leng, A. Vishnyakov, C.B. Arnold, Swelling and softening of lithium-ion battery separators in electrolyte solvents, *J. Power Sources* 294 (2015) 167-172.
- [69] H.-K. Park, B.-S. Kong, E.-S. Oh, Effect of high adhesive polyvinyl alcohol binder on the anodes of lithium ion batteries, *Electrochem. Commun.* 13 (2011) 1051-1053.
- [70] J.-H. Lee, U. Paik, V.A. Hackley, Y.-M. Choi, Effect of poly(acrylic acid) on adhesion strength and electrochemical performance of natural graphite negative electrode for lithium-ion batteries, *J. Power Sources* 161 (2006) 612-616.
- [71] M. Wu, X. Xiao, N. Vukmirovic, S. Xun, P.K. Das, X. Song, P. Olalde-Velasco, D. Wang, A.Z. Weber, L.-W. Wang, V.S. Battaglia, W. Yang, G. Liu, Toward an Ideal Polymer Binder Design for High-Capacity Battery Anodes, *J. Am. Chem. Soc.* 135 (2013) 12048-12056.
- [72] M.H.T. Nguyen, E.-S. Oh, Improvement of the characteristics of poly(acrylonitrile-butylacrylate) water-dispersed binder for lithium-ion batteries by the addition of acrylic acid and polystyrene seed, *J. Electroanal. Chem.* 739 (2015) 111-114.
- [73] M.-H. Ryou, J. Kim, I. Lee, S. Kim, Y.K. Jeong, S. Hong, J.H. Ryu, T.-S. Kim, J.-K. Park, H. Lee, J.W. Choi, Mussel-Inspired Adhesive Binders for High-Performance Silicon Nanoparticle Anodes in Lithium-Ion Batteries, *Adv. Mater.* 25 (2013) 1571-1576.
- [74] H. Zhao, Y. Wei, R. Qiao, C. Zhu, Z. Zheng, M. Ling, Z. Jia, Y. Bai, Y. Fu, J. Lei, X. Song, V.S. Battaglia, W. Yang, P.B. Messersmith, G. Liu, Conductive Polymer Binder for High-Tap-Density Nanosilicon Material for Lithium-Ion Battery Negative Electrode Application, *Nano Lett.* 15 (2015) 7927-7932.
- [75] S.R. Higgins, C.M. Eggleston, K.G. Knauss, C.O. Boro, A hydrothermal atomic force microscope for imaging in aqueous solution up to 150 °C, *Rev. Sci. Instrum.* 69 (1998) 2994-2998.

- [76] M.J. Higgins, R. Proksch, J.E. Sader, M. Polcik, S. Mc Endoo, J.P. Cleveland, S.P. Jarvis, Noninvasive determination of optical lever sensitivity in atomic force microscopy, *Rev. Sci. Instrum.* 77 (2006) 013701.
- [77] H.J. Butt, M. Jaschke, Calculation of thermal noise in atomic force microscopy, *Nanotechnology* 6 (1995) 1.
- [78] R. Proksch, T.E. SchÄffler, J.P. Cleveland, M.B.V. R C Callahan and, Finite optical spot size and position corrections in thermal spring constant calibration, *Nanotechnology* 15 (2004) 1344.
- [79] H.C. Liu, C.-C. Tuan, A.A. Bakhtiary Davijani, P.-H. Wang, H. Chang, C.-P. Wong, S. Kumar, Rheological behavior of polyacrylonitrile and polyacrylonitrile/lignin blends, *Polymer* 111 (2017) 177-182.
- [80] I. Cendoya, D. López, A. Alegría, C. Mijangos, Dynamic mechanical and dielectrical properties of poly(vinyl alcohol) and poly(vinyl alcohol)-based nanocomposites, *J. Polym. Sci. Pt. B: Polym. Phys.* 39 (2001) 1968-1975.
- [81] H. Montès, K. Mazeau, J.Y. Cavailé, Secondary Mechanical Relaxations in Amorphous Cellulose, *Macromolecules* 30 (1997) 6977-6984.
- [82] M. Varenberg, I. Etsion, G. Halperin, An improved wedge calibration method for lateral force in atomic force microscopy, *Rev. Sci. Instrum.* 74 (2003) 3362-3367.
- [83] B.C. Tran Khac, K.-H. Chung, Quantitative assessment of contact and non-contact lateral force calibration methods for atomic force microscopy, *Ultramicroscopy* 161 (2016) 41-50.
- [84] S. Perni, P. Prokopovich, C. Piccirillo, J. Pratten, I.P. Parkin, M. Wilson, Toluidine blue-containing polymers exhibit potent bactericidal activity when irradiated with red laser light, *J. Mater. Chem.* 19 (2009) 2715-2723.
- [85] B. Narasimhan, N.A. Peppas, Disentanglement and reptation during dissolution of rubbery polymers, *J. Polym. Sci. Pt. B: Polym. Phys.* 34 (1996) 947-961.
- [86] J.W. Rhim, H.S. Hwang, D.S. Kim, H.B. Park, C.H. Lee, Y.M. Lee, G.Y. Moon, S.Y. Nam, Aging effect of poly(vinyl alcohol) membranes crosslinked with poly(acrylic acid-co-maleic acid), *Macromol. Res.* 13 (2005) 135-140.
- [87] S.K. Mallapragada, N.A. Peppas, Crystal unfolding and chain disentanglement during semicrystalline polymer dissolution, *AICHE J.* 43 (1997) 870-876.
- [88] S.K. Mallapragada, N.A. Peppas, Dissolution mechanism of semicrystalline poly(vinyl alcohol) in water, *J. Polym. Sci. Pt. B: Polym. Phys.* 34 (1996) 1339-1346.
- [89] D. Kekuda, H.-S. Lin, M. Chyi Wu, J.-S. Huang, K.-C. Ho, C.-W. Chu, The effect of solvent induced crystallinity of polymer layer on poly(3-hexylthiophene)/C70 bilayer solar cells, *Sol. Energy Mater. Sol. Cells* 95 (2011) 419-422.
- [90] N. Yabuuchi, K. Shimomura, Y. Shimbe, T. Ozeki, J.-Y. Son, H. Oji, Y. Katayama, T. Miura, S. Komaba, Graphite-Silicon-Polyacrylate Negative Electrodes in Ionic Liquid Electrolyte for Safer Rechargeable Li-Ion Batteries, *Adv. Energy Mater.* 1 (2011) 759-765.

- [91] V.S. Mangipudi, E. Huang, M. Tirrell, A.V. Pocius, Measurement of interfacial adhesion between glassy polymers using the JKR method, *Macromol Symp.* 102 (1996) 131-143.
- [92] A.L. Weisenhorn, P. Maivald, H.J. Butt, P.K. Hansma, Measuring adhesion, attraction, and repulsion between surfaces in liquids with an atomic-force microscope, *Phys. Rev. B* 45 (1992) 11226-11232.
- [93] A.C. Hillier, S. Kim, A.J. Bard, Measurement of Double-Layer Forces at the Electrode/Electrolyte Interface Using the Atomic Force Microscope: Potential and Anion Dependent Interactions, *J. Phys. Chem.* 100 (1996) 18808-18817.
- [94] S.B. Velegol, B.E. Logan, Contributions of Bacterial Surface Polymers, Electrostatics, and Cell Elasticity to the Shape of AFM Force Curves, *Langmuir* 18 (2002) 5256-5262.
- [95] Y. Liang, N. Hilal, P. Langston, V. Starov, Interaction forces between colloidal particles in liquid: Theory and experiment, *Adv. Colloid Interface Sci.* 134-135 (2007) 151-166.
- [96] H.R. Hertz, *Über die Berührung fester elastischer Körper und Über die Harte*, *J. Reine Angew. Math.* 92 (1882) 156-171.
- [97] B. Bhushan, K.J. Kwak, S. Gupta, S.C. Lee, Nanoscale adhesion, friction and wear studies of biomolecules on silane polymer-coated silica and alumina-based surfaces, *J. R. Soc. Interface* 6 (2009) 719-733.
- [98] X. Liu, J. Song, D. Wu, J. Genzer, T. Theyson, O.J. Rojas, Surface and Friction Behavior of a Silicone Surfactant Adsorbed on Model Textiles Substrates, *Ind. Eng. Chem. Res.* 49 (2010) 8550-8557.
- [99] S.M. Pawde, D. Kalim, Influence of γ irradiation on the properties of polyacrylonitrile films, *J. Appl. Polym. Sci.* 110 (2008) 2569-2578.
- [100] M. Mahmood, H. Asiful, H. Yousef, Thermal and mechanical properties of poly(vinyl alcohol) plasticized with glycerol, *J. Appl. Polym. Sci.* 122 (2011) 3102-3109.
- [101] B. Miller-Chou, J.L. Koenig, A review of polymer dissolution, *Prog. Polym. Sci.* 28 (2003) 1223-1270.
- [102] S.W. Choi, J.R. Kim, Y.R. Ahn, S.M. Jo, E.J. Cairns, Characterization of Electrospun PVdF Fiber-Based Polymer Electrolytes, *Chem. Matter.* 19 (2007) 104-115.
- [103] W.J. Cooper, P.D. Krasicky, F. Rodriguez, Effects of molecular weight and plasticization on dissolution rates of thin polymer films, *Polymer* 26 (1985) 1069-1072.
- [104] L. Gong, M.H.T. Nguyen, E.-S. Oh, High polar polyacrylonitrile as a potential binder for negative electrodes in lithium ion batteries, *Electrochem. Commun.* 29 (2013) 45-47.
- [105] D. Mazouzi, Z. Karkar, C. Reale Hernandez, P. Jimenez Manero, D. Guyomard, L. Roué, B. Lestriez, Critical roles of binders and formulation at multiscales of silicon-based composite electrodes, *J. Power Sources* 280 (2015) 533-549.
- [106] S.F. Badylak, D.O. Freytes, T.W. Gilbert, Extracellular matrix as a biological scaffold material: Structure and function, *Acta Biomater.* 5 (2009) 1-13.

- [107] K.E. Kadler, C. Baldock, J. Bella, R.P. Boot-Handford, Collagens at a glance, *J. Cell Sci.* 120 (2007) 1955.
- [108] P. Fratzl, Collagen: Structure and Mechanics, an Introduction, in: P. Fratzl (Ed.) *Collagen: Structure and Mechanics*, Springer US, Boston, MA, 2008, pp. 1-13.
- [109] F. Kai, H. Laklai, V.M. Weaver, Force Matters: Biomechanical Regulation of Cell Invasion and Migration in Disease, *Trends Cell Biol.* 26 (2016) 486-497.
- [110] K.A. Jansen, A.J. Licup, A. Sharma, R. Rens, F.C. MacKintosh, G.H. Koenderink, The Role of Network Architecture in Collagen Mechanics, *Biophys. J.* 114 (2018) 2665-2678.
- [111] D.P. McDaniel, G.A. Shaw, J.T. Elliott, K. Bhadriraju, C. Meuse, K.-H. Chung, A.L. Plant, The Stiffness of Collagen Fibrils Influences Vascular Smooth Muscle Cell Phenotype, *Biophys. J.* 92 (2007) 1759-1769.
- [112] K.-H. Chung, A.K. Chen, C.R. Anderton, K. Bhadriraju, A.L. Plant, B.G. Bush, R.F. Cook, F.W. DelRio, Frictional properties of native and functionalized type I collagen thin films, *Appl. Phys. Lett.* 103 (2013) 143703.
- [113] Y.-l. Yang, S. Motte, L.J. Kaufman, Pore size variable type I collagen gels and their interaction with glioma cells, *Biomaterials* 31 (2010) 5678-5688.
- [114] J. Xie, M. Bao, S.M.C. Bruekers, W.T.S. Huck, Collagen Gels with Different Fibrillar Microarchitectures Elicit Different Cellular Responses, *ACS Appl. Mater. Interfaces* 9 (2017) 19630-19637.
- [115] M.W. Conklin, J.C. Eickhoff, K.M. Riching, C.A. Pehlke, K.W. Eliceiri, P.P. Provenzano, A. Friedl, P.J. Keely, Aligned Collagen Is a Prognostic Signature for Survival in Human Breast Carcinoma, *The American Journal of Pathology* 178 (2011) 1221-1232.
- [116] P.P. Provenzano, K.W. Eliceiri, J.M. Campbell, D.R. Inman, J.G. White, P.J. Keely, Collagen reorganization at the tumor-stromal interface facilitates local invasion, *BMC Med.* 4 (2006) 38.
- [117] R. Malik, P.I. Lelkes, E. Cukierman, Biomechanical and biochemical remodeling of stromal extracellular matrix in cancer, *Trends Biotechnol.* 33 (2015) 230-236.
- [118] G.C. Wood, M.K. Keech, The formation of fibrils from collagen solutions. 1. The effect of experimental conditions: kinetic and electron-microscope studies, *Biochem J* 75 (1960) 588-598.
- [119] E.L. Mertz, S. Leikin, Interactions of Inorganic Phosphate and Sulfate Anions with Collagen, *Biochemistry* 43 (2004) 14901-14912.
- [120] M. Asgari, N. Latifi, H.K. Heris, H. Vali, L. Mongeau, In vitro fibrillogenesis of tropocollagen type III in collagen type I affects its relative fibrillar topology and mechanics, *Sci. Rep.* 7 (2017) 1392.
- [121] S.Z. Yow, C.H. Quek, E.K.F. Yim, C.T. Lim, K.W. Leong, Collagen-based fibrous scaffold for spatial organization of encapsulated and seeded human mesenchymal stem cells, *Biomaterials* 30 (2009) 1133-1142.

- [122] Y.-S. Youn, S. Kim, Real-time atomic force microscopy imaging of collagen fibril under ultraviolet irradiation, *J. Ind. Eng. Chem.* 42 (2016) 15-18.
- [123] C.A. Grant, D.J. Brockwell, S.E. Radford, N.H. Thomson, Tuning the elastic modulus of hydrated collagen fibrils, *Biophys. J.* 97 (2009) 2985-2992.
- [124] M. Franchi, V. Ottani, R. Stagni, A. Ruggeri, Tendon and ligament fibrillar crimps give rise to left-handed helices of collagen fibrils in both planar and helical crimps, *J. Anat.* 216 (2010) 301-309.
- [125] T. Gutsman, G.E. Fantner, M. Venturoni, A. Ekani-Nkodo, J.B. Thompson, J.H. Kindt, D.E. Morse, D.K. Fygenson, P.K. Hansma, Evidence that Collagen Fibrils in Tendons Are Inhomogeneously Structured in a Tubelike Manner, *Biophys. J.* 84 (2003) 2593-2598.
- [126] I.N. Sneddon, The relation between load and penetration in the axisymmetric boussinesq problem for a punch of arbitrary profile, *Int. J. Eng. Sci.* 3 (1965) 47-57.
- [127] K. Franke, J. Sapudom, L. Kalbitzer, U. Anderegg, T. Pompe, Topologically defined composites of collagen types I and V as in vitro cell culture scaffolds, *Acta Biomater.* 10 (2014) 2693-2702.
- [128] J. Sapudom, L. Kalbitzer, X. Wu, S. Martin, K. Kroy, T. Pompe, Fibril bending stiffness of 3D collagen matrices instructs spreading and clustering of invasive and non-invasive breast cancer cells, *Biomaterials* 193 (2019) 47-57.
- [130] S. Oh, Q.D. Nguyen, K.-H. Chung, H. Lee, Bundling of collagen fibrils using sodium sulfate for the biomimetic cell culturing, Manuscript submitted for publication (2019).